REPORT DOCUMENTATION PAGE

Form Approved
OMB No. 0704-0188

Public reporting burden for this collection of information is estimated to average 1 hour per response, including the time for reviewing instructions, searching existing data sources, gathering and maintaining the data needed, and completing and reviewing the collection of information. Send comments regarding this burden estimate or any other aspect of this collection of information, including suggestions for reducing this burden, to Washington Headquarters Services, Directorate for Information Operations and Reports, 1215 Jefferson Davis Highway, Suite 1204, Arlington, VA 22202-4302, and to the Office of Management and Budget, Paperwork Reduction Project (0704-0188), Washington, DC 20503.

1. AGENCY USE ONLY (Leave Blank)	2. REPORT DATE 10-20-97	3. REPORT TYPE AND DATES COVERED Final Technical Report

4. TITLE AND SUBTITLE

Smart wall for control of the burst cycle of longitudinal vortices in turbulent boundary layers.

5. FUNDING NUMBERS

DAAH04-93-G-0212

6. AUTHORS

T. C. Corke (PI)

7. PERFORMING ORGANIZATION NAME(S) AND ADDRESS(ES)

Illinois Institute of Technology
3300 S. Federal St.
Chicago, IL 60616

8. PERFORMING ORGANIZATION REPORT NUMBER

TCC-1-97

9. SPONSORING / MONITORING AGENCY NAME(S) AND ADDRESS(ES)

U.S. Army Research Office, 4300 S. Miami Blvd.
P.O. Box 12212, Research Triangle Park, NC 27709

10. SPONSORING / MONITORING AGENCY REPORT NUMBER

ARO 32111.1-EG-SM

11. SUPPLEMENTARY NOTES

12a. DISTRIBUTION / AVAILABILITY STATEMENT

Approved for public release; distribution unlimited.

12b. DISTRIBUTION CODE

13. ABSTRACT (Maximum 200 words)

This work was aimed at developing a "smart wall" through the integration of an optical-sensor pressure transducer array and an array of miniature magnetic actuators. The pressure transducer array corresponded to one mirror of an interferometer. This mirror was a thin, flexible sheet on which a reflective layer had been vapor deposited. The sheet overlayed an array of small closely spaced holes in the wall surface. The instantaneous pressure was determined over each hole by the spacing of Moire fringes. The fringe patterns over each hole were simultaneously acquired by a ccd-camera (viewing the full field) and frame-grabber connected to a host computer. The processing involved converting the fringe pattern to pressures, using a neural network, and performing spatial filtering to highlight features associated with longitudinal vortices (large streamwise wave lengths and short spanwise wave lengths). As a compliment to this, a 1-D array of hot-wire sensors were acquired for the same flow conditions. 2-D space-time analysis of the hot-wire data series were used to categorize the most effective actuator settings. These results were compared to those from the optical pressure sensor array. Bridging the two experiments was the development of software for 2-D Fourier, frequency/wave number analysis of the data series. The final part of the work was the development of a wall element which could introduce spanwise-periodic distortions in the wall surface. This consisted of a flexible silicon sheet which covered narrow electro-magnetic strips. The strips formed a 1-D array with a spanwise spacing which was suitable for the spanwise scale of streamwise vortices which formed in the flow. The strips deflected in response to a computer output which was designed to produce a standing pattern in the flow. The optimum number, spacing and amplitude of activated strips was investigated based on response of the flow as seen by the hot-wire and pressure arrays.

14. SUBJECT TERMS

vortex control, optical pressure sensor, wall control, flexible wall, boundary layer control

15. NUMBER OF PAGES 65

16. PRICE CODE

17. SECURITY CLASSIFICATION OF REPORT UNCLASSIFIED	18. SECURITY CLASSIFICATION OF THIS PAGE UNCLASSIFIED	19. SECURITY CLASSIFICATION OF ABSTRACT UNCLASSIFIED	20. LIMITATION OF ABSTRACT UL

NSN 7540-01-280-5500

Standard Form 298 (Rev. 2-89)
Prescribed by ANSI Std. Z39-1
298-102

DTIC QUALITY INSPECTED 3

Final Report

Grant Number DAAH04-93-G-0212

Smart-Wall for Control of the Burst Cycle of Longitudinal Vortices in Turbulent Boundary Layers

by

Thomas C. Corke (PI)

Fluid Dynamics Research Center

Illinois Institute of Technology

Mechanical, Materials & Aerospace Enginering Department

Chicago, Il 60616

(312) 567-3184 (tel)   (312) 567-7230 (fax)

Email: corke@mae.iit.edu

October, 1997

1

Contents

1 Abstract

This work was aimed at developing a "smart wall" through the integration of an optical-sensor pressure transducer array and an array of miniature magnetic actuators. The pressure transducer array corresponded to one mirror of an interferometer. This mirror was a thin, flexible sheet on which a reflective layer had been vapor deposited. The sheet overlayed an array of small closely spaced holes in the wall surface. The instantaneous pressure was determined over each hole by the spacing of Moire fringes. The fringe patterns over each hole were simultaneously acquired by a ccd-camera (viewing the full field) and frame-grabber connected to a host computer. The processing involved converting the fringe pattern to pressures, using a neural network, and performing spatial filtering to highlight features associated with longitudinal vortices (large streamwise wave lengths and short spanwise wave lengths). As a compliment to this, a 1-D array of hot-wire sensors were acquired for the same flow conditions. 2-D space-time analysis of the hot-wire data series were used to categorize the most effective actuator settings. These results were compared to those from the optical pressure sensor array. Bridging the two experiments was the development of software for 2-D Fourier, frequency/wave number analysis of the data series. The final part of the work was the development of a wall element which could introduce spanwise-periodic distortions in the wall surface. This consisted of a flexible silicon sheet which covered narrow electro-magnetic strips. The strips formed a 1-D array with a spanwise spacing which was suitable for the spanwise scale of streamwise vortices which formed in the flow. The strips deflected in response to a computer output which was designed to produce a standing pattern

in the flow. The optimum number, spacing and amplitude of activated strips was investigated based on response of the flow as seen by the hot-wire and pressure arrays.

2   Background and Motivation

A common feature in experiments and large-scale computations in turbulent channel flows and boundary layer flows, with or without wall curvature, is the presence of spanwise concentrations of streamwise vorticity. Although there appears to be no single theory to account for the focusing of streamwise vorticity into the wall layer, its existence is undeniable. The underlying assumption is that a substantial amount of turbulence production is due to the instability of longitudinal vortices ("streaks") that are prevalent in the near-wall region of turbulent boundary layers. Understanding the mechanisms behind this is important to controlling viscous drag and in predicting and controlling surface heat transfer. This is relevant to such technological areas as decreasing the base drag on the wings and fuselage of aircraft, and increasing the efficiency of turbo-jet engines by reducing the heat transfer to turbine blades.

Passive approaches to controlling the wall "streaks" in turbulent boundary layers already has had some success. We assume that these vortices can come singly or as co-rotating or counter-rotating pairs of equal or unequal strength, and that they exist in the regions of the highest mean flow shear. Singly, such vortices are inherently unstable when perturbed by small disturbances. When they come in pairs, a mutual interaction can lead to significant modification of the mean flow

which can lead to local mean velocity inflections and the generation of small scale turbulence through an inviscid Rayleigh-type instability.

In understanding the physics of this process, it is relevant to consider also transitional boundary layers. For example in boundary layers without wall curvature, Hall and Smith (1991) have performed asymptotic analysis on the nonlinear interaction and focusing of vorticity of near-planar waves and longitudinal vortices in a channel flow. This is of a type which originates due to a warping of concentrated ω_z vortex tubes perturbed by large amplitude fluctuations. Coherent longitudinal vortices also arise at initially low amplitudes due to the mutual interaction of pairs of traveling oblique wave pairs (of equal-opposite wave angles, in wave number format $(1, \pm 1)$). Through a nonlinear interaction, these produce a pair of stationary counter-rotating vortices $(0, \pm 2)$). This process as it applies to subharmonic mode transition in boundary layers has been experimentally recorded by Corke and Mangano (1989), and was found to agree well with the analysis of Mankbadi (1992) and Herbert (review article, 1988).

Another boundary layer flow in which the transition to turbulence is dominated by longitudinal vortices is on highly swept wings where a cross-flow component of velocity exists. In this case coherent co-rotating longitudinal vortices arise due to a cross-flow instability. The stages of development leading to the breakdown of stationary cross-flow vortices have been beautifully rendered in the flow visualization records of Kohama (1984). Linear stability analysis of the cross-flow instability on a rotating disk, which is a close flow analog to the swept wing, has been done by Malik, Wilkinson and Orsag (1981). This has recently been extended to include

6

nonlinear effects in a PSE version by Balakumar and Malik (1991). Asymptotic approaches have also been used by Bassom and Hall (1989, 1990) to study the interaction of stationary cross-flow vortices and traveling disturbances.

A final example of a boundary layer flow which is dominated by longitudinal vorticity is that which occurs on a concave curved wall. In this case a system of counter-rotating longitudinal vortices arise due to the Gortler instability. Analysis concerning the onset of three-dimensionality and time dependent motions for large amplitude Gortler vortices has been recently performed by Bassom and Seddougui (1989), Hall and Horseman (1990) and Bassom and Otto (1992).

Reviewing these cases in transitional boundary layer flows provides a framework for understanding the basic stages leading to the breakdown of a coherent flow module made up of longitudinal vortices. We believe that a majority of the basic mechanisms should be relevant in the wall region of turbulent boundary layers, and we have attempted to exploit these in designing a strategy for controlling the longitudinal vortex burst cycle in the fully turbulent regime.

3   Experimental Approach

Since we believe that the stability and breakdown of streamwise vortices in these different flows is a generic process with the same underlying physics, regardless of scale, we used as the basic flow module, the pairs of streamwise vortices produced by the nonlinear interaction of pairs of oblique waves in subharmonic transition of a 2-D boundary layer. This flow offered a number of advantages:

7

1. It provided an order of magnitude larger scale, compared to a fully turbulent boundary layer, with which we could develop the experimental tools without the added difficulties posed by extremely small scale.

2. We had the experimental setup (see Corke & Mangano, 1989; and Corke & Gruber, 1996) with which we could control the initial conditions of oblique-mode (subharmonic) transition in order to repeatable control the strength and location of streamwise vortices which arise from the nonlinear interaction of the excited oblique waves.

With our decision to use the controlled 2-D boundary layer transition as the prototypical flow with which to study methods of detection and control of stream-wise vortices, the research directions were subsequently broken down into **four** categories:

1. **Optical Pressure Sensor:** Since we expected that the concentrated vorticity associated with the wall-layer longitudinal vortices would induce a local pressure imprint at the wall, one direction was to develop a 2-D pressure sensor array. We chose to base the design on the use of a Moire interferometer. The optical approach was taken because of its extreme sensitivity, which was important with potentially small diaphragms, and because we envisioned the advantages of using a ccd-camera as a parallel input device to provide fast, global/spatial data acquisition.

2. **Wall Actuator:** The wall actuator was intended to introduce a standing pattern of spanwise fluctuations in the wall surface height. The intention was

to provide a spanwise scale to the streamwise vortices which would affect their strength and stability. The requirements of the actuator was that it have low mass and damping to give sufficient frequency response, and that deflections would be controllable with low power outputs from a parallel output buffer on a digital computer.

3. **Wall-velocity Array:** Because the optical sensor array would require complete development, we also utilized a 1-D array of hot-wire sensors. The sensors were located close to the wall and used as a "binary" indicator of the flow state which included the streamwise vortices. The development of the processing techniques of the pseudo 2-D (space-time) information ultimately benefited the processing of the 2-D pressure array. The information from the hot-wire array also provided an important check on the optical pressure sensor output.

4. **Analysis Software:** The analysis software was needed to perform tasks such as Moire fringe identification and pressure classification, 2-D frequency/wave number analysis of data series obtained from the hot-wire or pressure arrays, and flow-state classification. In terms of the space or time series, the process of filter reconstruction was to be exploited to improve the spatial resolution of the data. The development and testing of these software was made into a separate task so that it would be available when the hardware parts of the experiment were completed. Part of this development was covered by a separate AASERT grant.

The steps in the development of these four aspects of the work, and the experimental results which came as an outcome, are presented in the following sections.

4 Optical Pressure Sensor

The details of the pressure sensor are contained in the Ph.D. thesis of Parham Piroozan. A copy of the thesis is included as a separate attachment to this report.

The optical pressure transducer was based on measuring the deflection of an array of diaphragms using a Moire interferometer. The diaphragms were formed by stretching an elastic membrane over an array of holes in a plate which was set into the boundary layer wall. The membrane was vapor deposited with a thin reflective metal coating. The mechanical characteristics of the diaphragm (material, thickness and tension) were all found to be important, and a technological challenge in the development of the system.

4.1 Transducer Construction

The pressure surface was constructed from a circular disk which was designed to be inserted into the boundary layer plate, from the back side, and be aligned so that there was a smooth transition between the measurement side of the plate and disk surfaces. A schematic drawing is shown in Figure 1. The disk was constructed from a cast Stainless-steel alloy plate. This type of plate has very few residual stresses which minimized distortions following machining. After machining, the plate was then diamond lapped flat to within 1/4-wavelength of Helium light, and polished to a 0.5RA finish. This surface quality was important in obtaining good quality fringes.
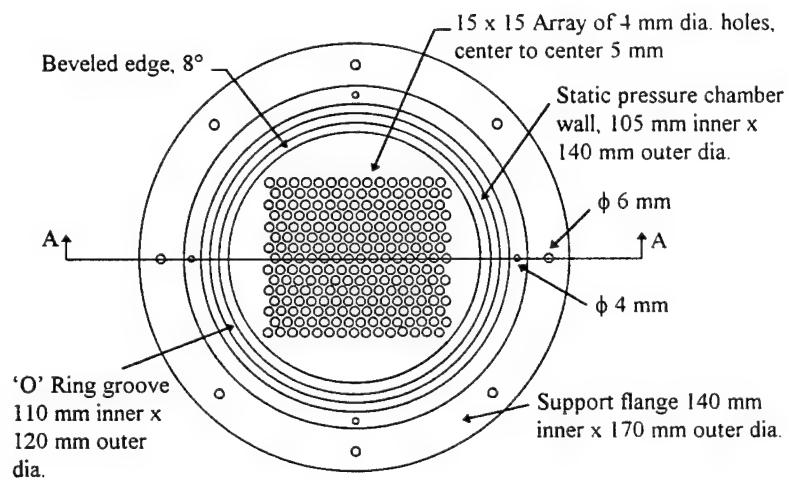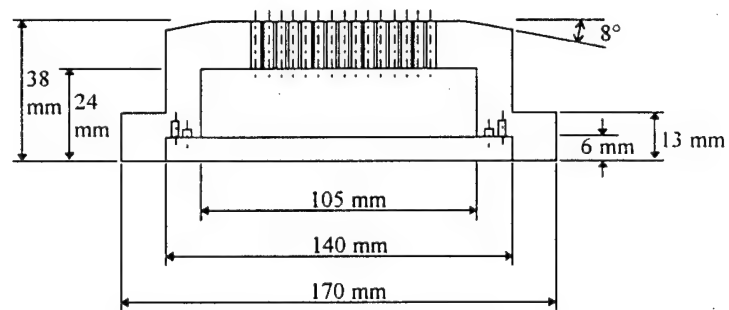
10

AA

Figure 1: Schematic drawing of stainless-steel disk with 15×15 array of holes for optical pressure sensor.

For the pressure sensors, a 15×15 array of holes were drilled through the disk. The diameter and spacing of the holes were selected to give a spatial resolution of approximately 4 holes per spanwise wave length of the streamwise vortex mode in the experiment. The holes were spaced evenly in the spanwise and streamwise directions. All of the holes communicated through a common closed cavity which was inside the disk. The cavity was pressurized and kept to match the local wind tunnel static pressure so that the diaphragms primarily measured the local pressure fluctuations.

The measurement surface of the disk was covered with a thin membrane. It was necessary to stretch the membrane before it was bonded to the surface. To facilitate this, an 8° bevel was machined around the edge of the disk. The membrane was bonded only along the beveled region.

The modulus of elasticity of the material used for the membrane had a crucial role in the performance of the optical transducer. We explored many different materials. In the end we chose nitrocellulose for the pressure range of ±0.05psi, and silicone (Dow Corning controlled volatility silicone) for lower pressure ranges of ±0.001psi. The mechanical properties of these two materials is given in Table 2.1 of Piroozan's thesis. Of these two, the silicon proved to be the most difficult to consistently coat a reflective surface. For that reason we primarily used nitrocellulose membranes.

The thickness of the membrane is also important in setting the useful pressure range of the sensor. For our measurements with the nitrocellulose membranes, the thickness was 1.5microns (±0.1μm). The reflective coating on the membranes
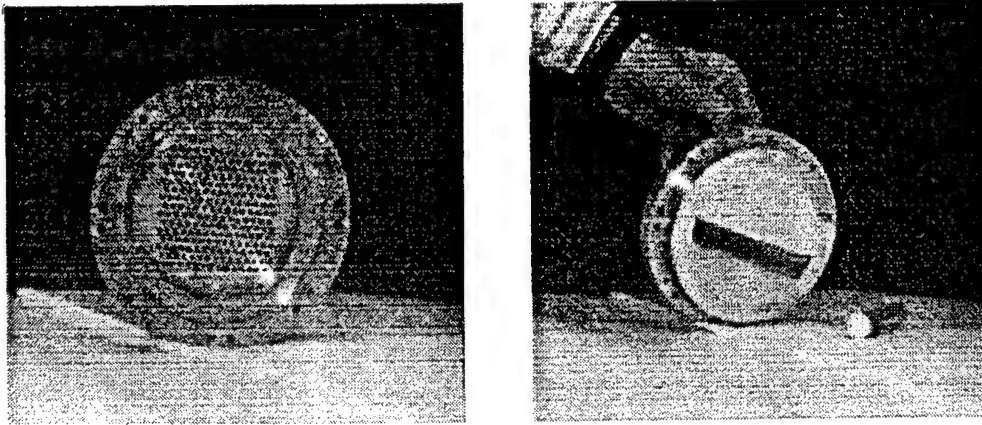
Figure 2: Photographs of back (left) and measurement (right) sides of optical pressure sensor.

was a 300 to 350 Angstroms thick coating of aluminum. The aluminum coating was not expected to change the mechanical properties of the diaphragm. These coatings gave a reflectivity of approximately 88%, which we found to be good enough for our applications. Silver would have been better, but approximately two-times more costly. Figure 2. shows the optical pressure sensor disk from the back (left) and measurement (right) sides after being covered by the silvered nitrocellulose membrane.

A membrane theory analysis was conducted on a idealized sensor. This was used to determine the relationship between the mechanical properties of the material, its thickness, and the amount of pre-tensioning applied to the material when it was bonded to the surface. The results are given in Table 1 (below). We note that the silicon is more suitable for the lower pressures. Manufacturing limitations however required that the silicon sheets be made thicker than the nitrocellulose sheets. This resulted in using a lower amount of pre-tensioning. The lower the amount of pre-tensioning, the less (in theory) the sheet behaved as a membrane. This was an

13

Table 1: Design Parameters for Diaphragms.

P_{max} (psi)	Material	Tension (lbs/in)	Thickness (micron)	Strain (in/in)
0.0005	silicone	0.01	51	0.010
0.001	silicone	0.02	51	0.020
0.001	silicone	0.02	100	0.010
0.001	silicone	0.02	200	0.005
0.01	nitrocellulose	0.2	1.5	0.017
0.05	nitrocellulose	1.00	8	0.016

adverse effect which led to our greater use of the thinner nitrocellulose membranes, which had a larger amount of pre-tensioning.

4.2   Optical Setup

An optical Moire interferometer was used to visualize fringes proportional to the slope of each of the diaphragms over each of the 15×15 array of holes in the disk in the boundary layer wall. Five possible optical setups were examined, along with derivations of the equations governing the relation between the fringe spacing and membrane deflection. The complete analysis is contained in the thesis by Paroozan (1997). In this report we summarize the final setup.

A schematic drawing of the optical setup is shown in Figure 3. A photograph of the setup as it was used in the wind tunnel measurements, is shown in Figure 4. This shows a **reflection Moire shear interferometer**. The setup uses a monochromatic collimated light source which is oblique to the object and makes an angle α with the normal to the plane of the pressure sensor. This design uses two gratings. The amount of shear is controlled by the distance between the two gratings. In this setup, each grating is placed on either side of the optical rail. A
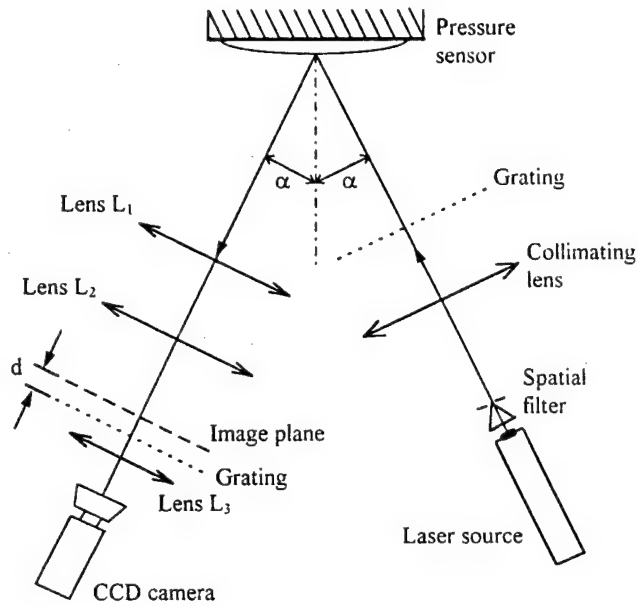
14

Figure 3: Schematic of optical setup which gives high sensitivity and controlled shear.

telecentric system of lenses (L_1 and L_2 are identical and have the same focal length and diameter) is used to reproduce the pressure sensor at the focal point of lens L_2. The pressure sensor and lens L_2 are located at the focal point of lens L_1. The second grating (on the reflection side) is located a distance d from the image plane. Both gratings have a density of 1000lines/in. Lens L_3 has a short focal length and is used to filter the multiple orders and focus orders 0 and +1 or -1 onto the CCD camera image plane. Since slope fringes in this case are formed by interference of only two orders, fringes have a high visibility.

4.3 Sensitivities and Limits

The intensity sensitivity in this design is

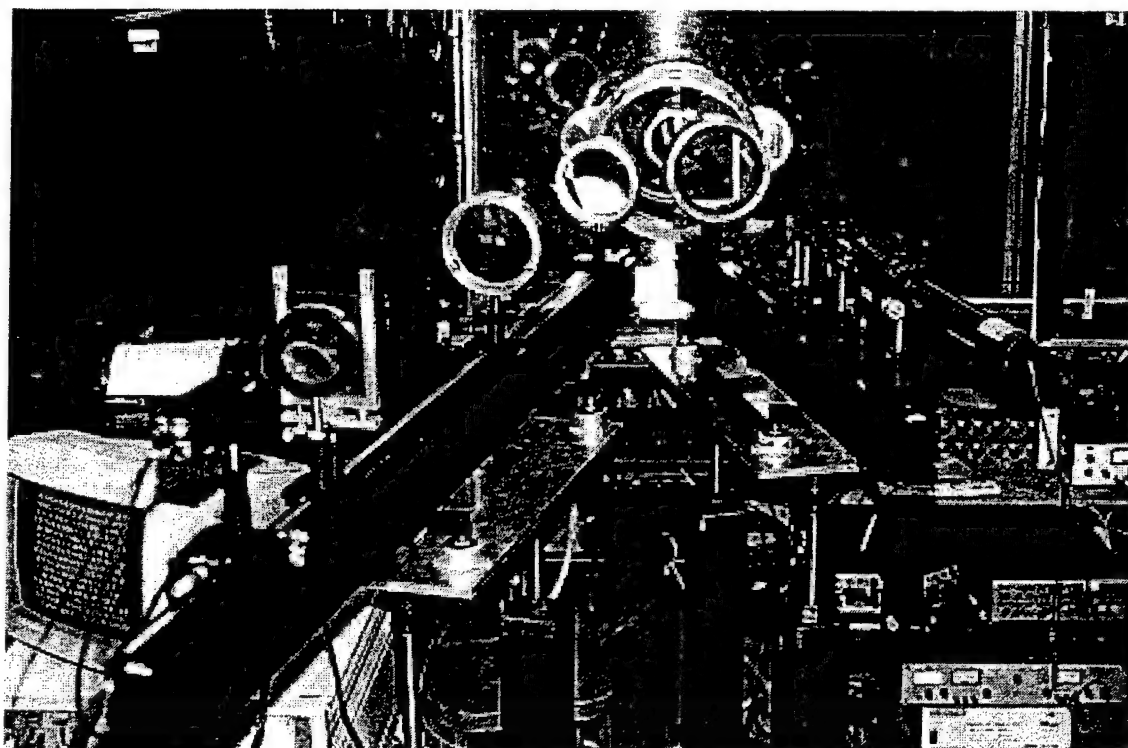$$\text{Sensitivity} = \frac{p_n}{2d}$$

15

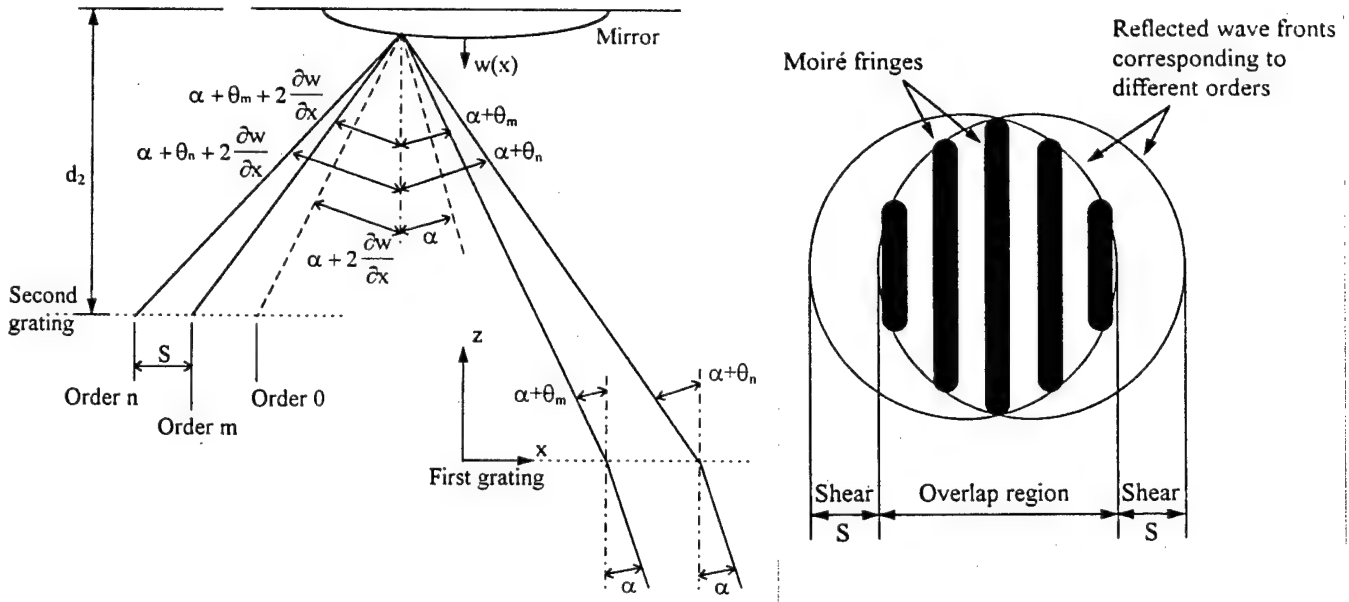Figure 4: Photograph of optical setup shown schematically in Figure 3.

Figure 5: Schematic showing a representation of the shear interferometer (left), and regions where Moire fringes form (right).

where p_n is the pitch of the grating, normal to the optical axis, and d is the distance between the image plane and the second grating, as seen in Figure 3. The shear in the wave front, S, is given by

$$S = \frac{d\lambda}{p_n}$$

where λ is the wave length of the incident light.

The amount of shear (or shift) of the wave front refers to the distance between the order 0 and order n^{th} interference on the second grating. This is illustrated in the top part of Figure 5, and is a measure of the performance of the optical system. Each term (with different n and m) gives a pattern with different sensitivity. The lowest sensitivity corresponds to $|n - m| = 1$. High sensitivity is desired for small slope measurements.

The amount of shear is however limited by the size of the object, in this case,
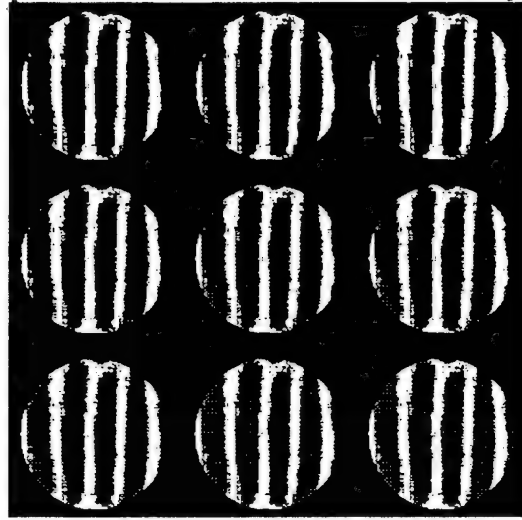
Figure 6: Constant slope Moire fringes over 3×3 version of the pressure sensor. Note a circular mask was digitally applied.

the diameter of the diaphragm. This is illustrated in the bottom part of Figure 5. The larger the shear value used, the smaller the actual object size becomes with which to form the Moire fringes that contain the slope information. This is because the fringes are formed in the overlap region of the object and the shifted front. The heart of the technique is to find the ideal compromise between increasing sensitivity and accuracy in reading the fringe frequency.

Figure 6 shows a sample of the fringes recorded over a 3×3 region of the pressure sensor. Here, only the fringes are recorded with the optical system. This was done by applying a circular mask with the image processing system used to acquire the image.

Analysis of the circular membrane gave the relationship between the maximum slope and maximum deflection as

$$\frac{\partial w}{\partial r} = \frac{2w_0}{a}$$

where w_0 is the maximum deflection at the center of the circular membrane and a is the sensor (hole) radius.. This leads to

$$w_0 = \frac{nap_n}{4d}$$

which also gives a relation for the membrane tension, T_0, as

$$T_0 = \frac{Pad}{np_n}$$

where P is the differential pressure on the diaphragm.

We utilized these equations to determine the optimum conditions for the optical sensor. The design of the hole diameter and spacing was set by the spanwise scale of the streamwise vortices. This gave a diameter of 4mm and a spacing between holes of 1mm. The 1mm spacing determines the maximum shear distance, S. Any larger value would mean that there would be an overlap of the images from one diaphragm to its neighbor. Using the other values of $p_n = 120$lines/in and $\lambda = 632.8$nm, the largest value of d is 334mm (13.1in).

We determine the maximum deflection of the membrane based on a hole radius $a = 2$mm, $d = 6$in and $n = 3$. This gave $w_0 = 2.08\mu$m. The value of n was selected to limit the number of fringes over a diaphragm to 6. Therefore to maintain this maximum number of fringes for this maximum displacement, the initial tension, T_0 becomes a parameter which can counter the choice of a design mean differential pressure, P. For example, a differential pressure of 5×10^{-4}psi would require $T_0 = 0.01$lb/in to satisfy these conditions.

4.4 Measurement of Pressure Fluctuations

Figure 4 showed a photograph of the final optical setup used in the wind tunnel experiments. The optics are carried on a pair of optical rails which form a V-shape with an angle, $\alpha = 13°$. The rail has vibration isolating feet which sit on a rigid base. The base is adjustable in height and angle. The light source was a 10mW Helium-Neon laser. The diameter of the laser beam was expanded from 0.95 to 150mm by using a microscope objective with a 63x magnification and a focal length of 2.94mm, a 5μm pin hole and a 762mm focal length collimating lens. The collimated light then passes through the first grating (1000lines/in) and is reflected off of the pressure sensor on the measurement wall of the wind tunnel. The light enters and leaves the tunnel through a 279mm diameter nonreflecting, optically flat glass which is mounted in the tunnel side-wall.

The reflected light passes through a telecentric lens system consisting of two identical lenses with diameters of 120mm and focal lengths of 600mm. This reproduces the pressure sensor at the focal point of the second lens. The second grating is placed a distance d from this focal length. This distance (d) controls the shear wave front and therefore the sensitivity. The maximum sensitivity occurred with $d = 40$mm, which gave the maximum possible shear of 1mm. The third lens, with a diameter of 76mm and focal length of 128.7mm was used to focus the fundamental harmonic (order +1 or -1) and order 0 onto the CCD camera object plane.

The resolution of the camera CCD array was such that a 24×24 pixel array covered each of the diaphragms. For a Sinc-function light intensity distribution of a fringe, 4 pixels were necessary for complete identification. This gave a maximum of
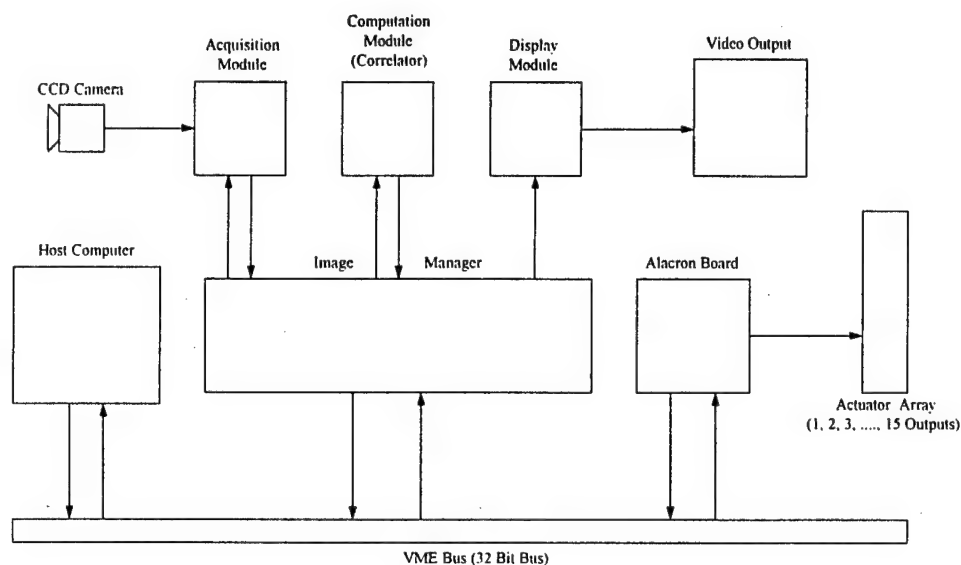
20

Figure 7: Schematic of hardware used to acquire and process Moire fringe images.

6 fringes per diaphragm. In order to compare the pressure measurements with the results from the 1×7 hot-wire array, we selected a 1×7 array of diaphragms. In this case we could use extra magnification and increase the size of the pixel array to 50×50. This increased the number of fringes per diaphragm to 12.

The fringe patterns over the individual diaphragms was recorded using a CCD camera. The camera and other hardware used in the image acquisition and processing are shown in Figure 7. The time resolution is determined by the scanning rate of the camera. In our case this was 1/60s in interlaced mode and 1/30s in noninterlaced mode. In theory, the streamwise vortices produced by the interaction of the oblique modes have zero frequency (standing modes). In practice, they are modulated by background disturbances so that their motion has a low frequency content above zero. As a result, these motions could be captured in the noninterlaced camera mode, which was capable of resolving frequencies (based on the Nyquest criteria) of up to 15Hz.

21

Table 2: Discretized Pressure Levels.

ΔP psi (N/m^2)	No. of Fringes per Sample Width	Discrete Pressure Level
-5×10^{-4} (-3.447)	8.5	1
-3×10^{-4} (-2.068)	8.3	2
-1×10^{-4} (-0.689)	8.1	3
1×10^{-4} (0.689)	7.9	4
3×10^{-4} (2.068)	7.7	5
5×10^{-4} (3.447)	7.5	6

4.5 Pressure Classification and Calibration

The fringe spacing or frequency was converted into the differential pressure through calibrated look-up table. For speed, the fringe spacing was discretized into 6 levels. These are given in Table 2.

The static calibration was done by applying a known differential pressure across the pressure array disk. This was done by pressurizing the cavity on the back side of the disk with pressures which were above or below atmospheric pressure. The wind tunnel side of the disk was exposed to atmospheric pressure. This was done with the disk installed in the tunnel to account for any imperfections or changes that might have occurred between bench testing and its use in experiments.

4.6 Neural Network Fringe Classification

As Table 2 indicates, we only resolved one full fringe number difference over the full range of calibration pressures. This required an **accurate** measurement of the number of fringes per sample width, and a conversion to the discrete pressure level which accounted for any nonidealized behavior of the diaphragms and optics. To satisfy these requirements, we utilized a neural network, in software, which was
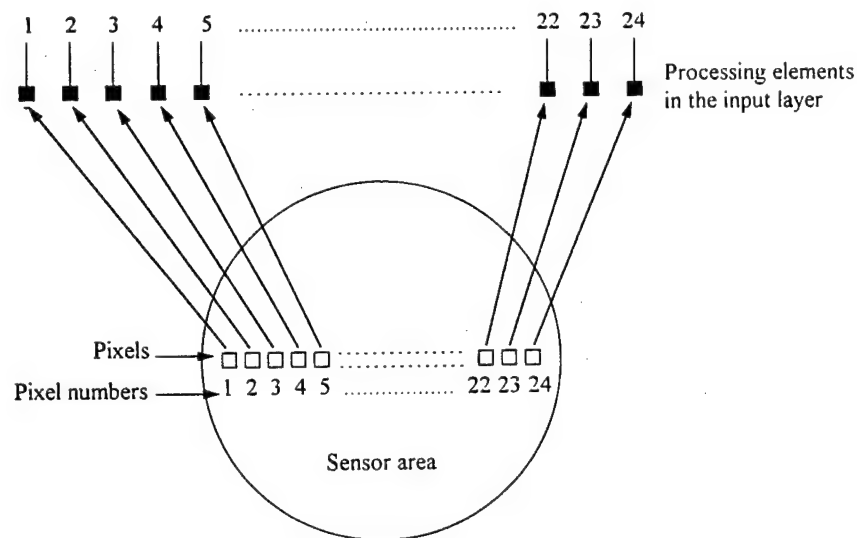
Figure 8: Schematic showing the input data from one element of the optical sensor to the input layer of the back-propagation neural network for pressure classification.

trained to recognize the fringe patterns and sort these according to the fringe spacing into discrete pressure levels.

With the neural network, a line of 24 pixels which cut across normal to the fringes of each sensor, were taken as the 24 processing elements in the input layer of the neural network. A schematic drawing of this is shown in Figure 8. The input levels of each pixel/element was 0 to 255 corresponding to the 8-bit intensity range provided by the camera.

The network was a back-propagation type which in addition to the 24 processing elements on the input, had 10 processing elements in a hidden layer, and 6 processing elements in the output layer, which were fully interconnected. The 6 processing elements in the output layer were the 6 discrete pressure levels. The input data was mapped to fall in the range of ±1 by normalizing by the maximum and minimum
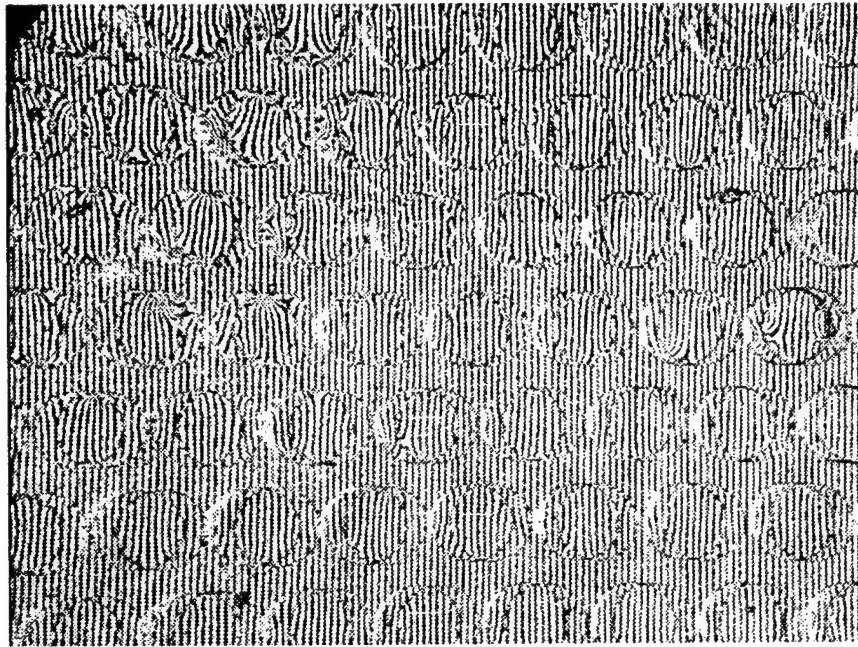
Figure 9: Recorded slope fringes for a no-flow condition in the wind tunnel.

values. A hyperbolic-tangent function was used as the "activation function". A normalized cumulative delta rule was used as the "learning rule." Approximately 350 training records were used at each applied pressure. Training was judged on the basis of the r.m.s. error. Typically the learning converged to an error level of 10%. Sources of errors were most typically due to fluctuations in the low pressure levels use for calibration. In testing, by applying known pressures, the trained neural network was found to give the correct pressure classification 85% of the time.

4.7   Sample Results

Sample results from the optical pressure array are given in this section. More detailed results involving all the measurements with different actuator conditions, will be presented in a later section.

Figure 9 shows a sample image of the fringe pattern over approximately one-

quarter of the 15×15 pressure array. This corresponds to a static case without flow. In this image we have not masked out the background which gives no information. As a result the shift in the image of each circular diaphragm due to the optical shear is evident. Recall that the fringes in the overlap regions are indicative of the diaphragm slope (see Figure 5). Ideally, all of the fringes should be vertical and straight. In most cases they were, although some nonideal behavior is noted. This was generally due to edge effects around the circular holes. For this reason, the interrogated regions were generally confined to the center portion of the diaphragm image. The use of the neural network was also beneficial in distinguishing the nonideal fringe shapes.

For the more detailed measurements, which were compared to the hot-wire array, we used a subset of the full pressure array. This corresponded to the 1×7 portion shown in Figure 10 (left). The sample image of the fringe patterns for this sub-element is shown in the right part of Figure 10. In this the white horizontal line near the center of the shifted image shows the sample region which provided the input to the neural network.

The experiment was run with the experimental conditions of Corke & Gruber (1996). This corresponded to a Falkner-Skan boundary layer with $\beta = -0.06$. Periodic disturbances were input upstream to excite subharmonic resonance of a pair of oblique modes with a spanwise wave length, λ_z, of 60.5mm. As a result of a nonlinear interaction, this resulted in a pair of counter-rotating streamwise vortices with λ_z=30.26mm. The seven sensors spanned 35mm.

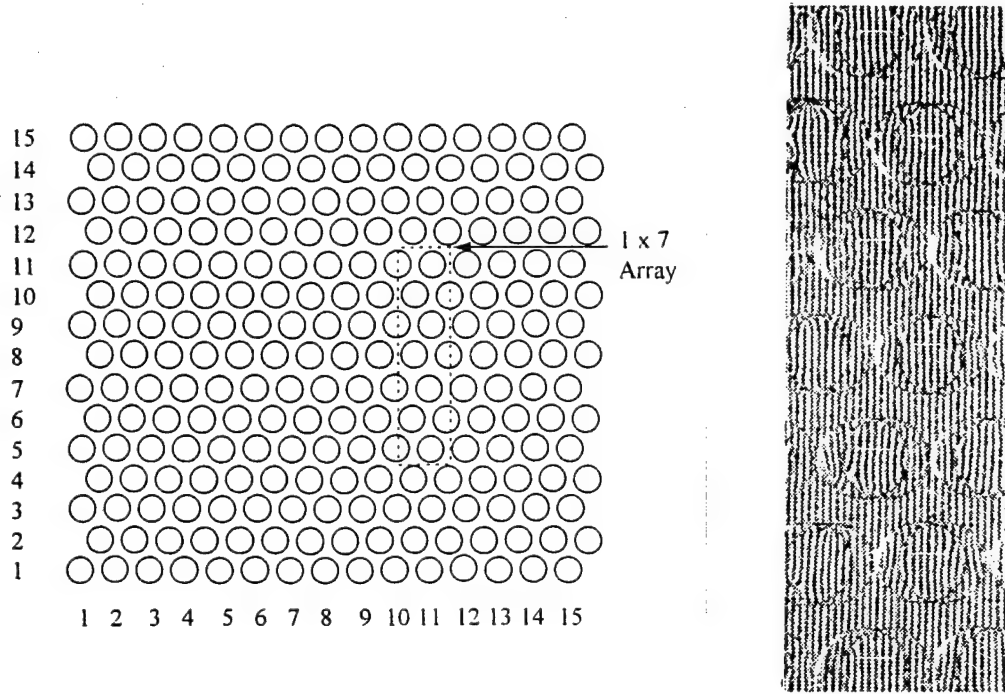Figures 11 and 12 show sample time series (bottom) and the corresponding av-

Figure 10: Relative location of 1 × 7 array (left) and corresponding slope fringes (right) used in the detailed analysis of the flow.

eraged frequency/wave-number spectrum taken from the 1 × 7 array portion of the optical pressure sensor. Figure 11 corresponds to the condition without oblique mode forcing. Figure 12 has the same basic flow but with oblique mode forcing. For the time series, the ordinate is the spanwise position made nondimensional with $\lambda_z/2$, the expected spanwise wave length of the streamwise vortex mode. The spanwise extent of the pressure sample is $\pm\lambda_z/2$ which encompasses $-0.5 \leq z/\lambda_z/2 \leq 0.5$ on the ordinate. The pressure is shown as iso-level contours. This shows the fluctuations about the mean which have been normalized by the minimum and maximum values.

The spectra on the top part of these figures has frequency on the abscissa and spanwise wave number on the ordinate. The maximum frequency is the Nyquist value of 7.5Hz. The spanwise wave number is nondimensionalized by multiplying it
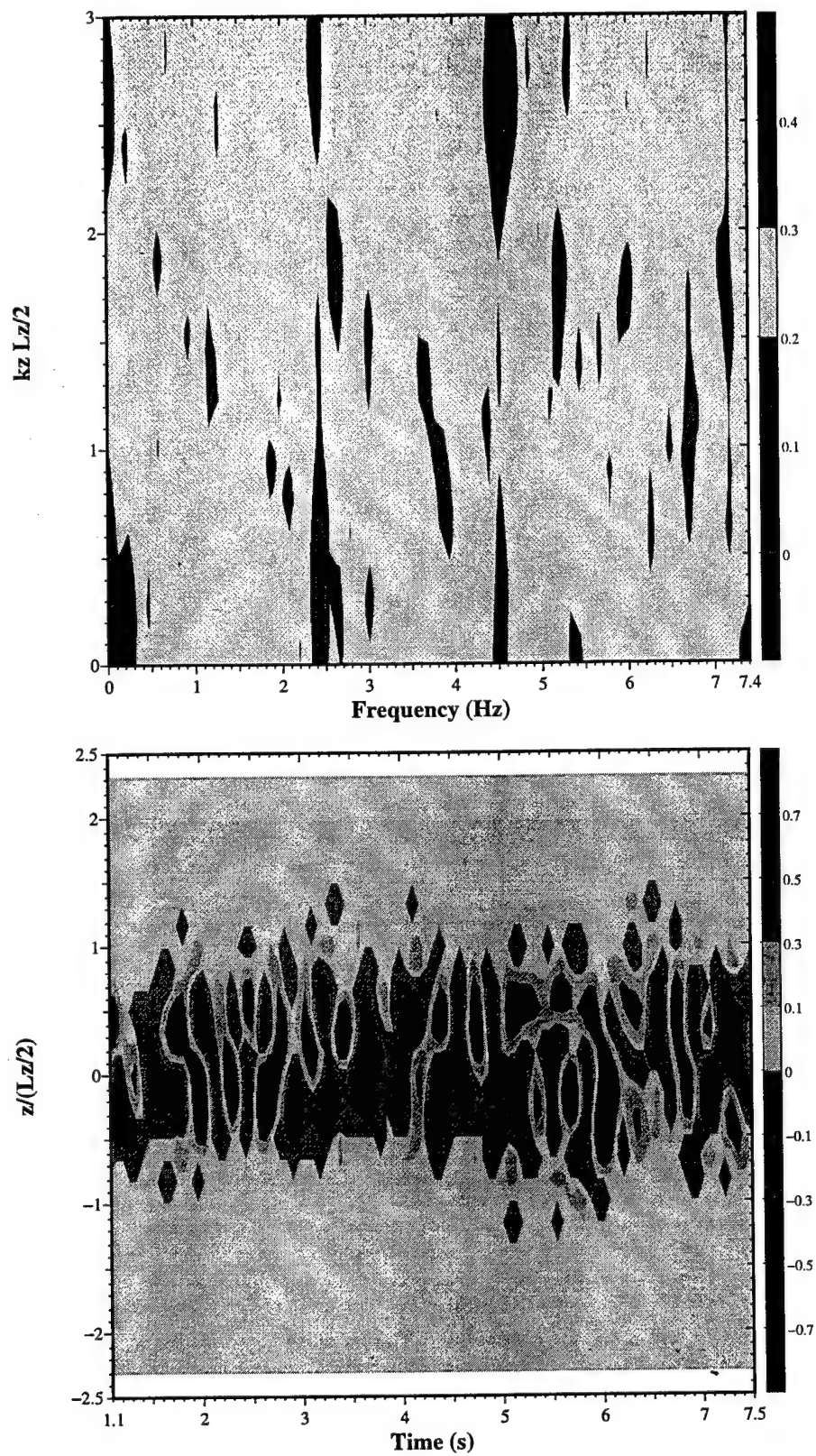
Figure 11: Frequency/spanwise wave number spectra (top) and sample time series (bottom) of wall pressure fluctuations in the boundary layer without 3-D mode forcing.
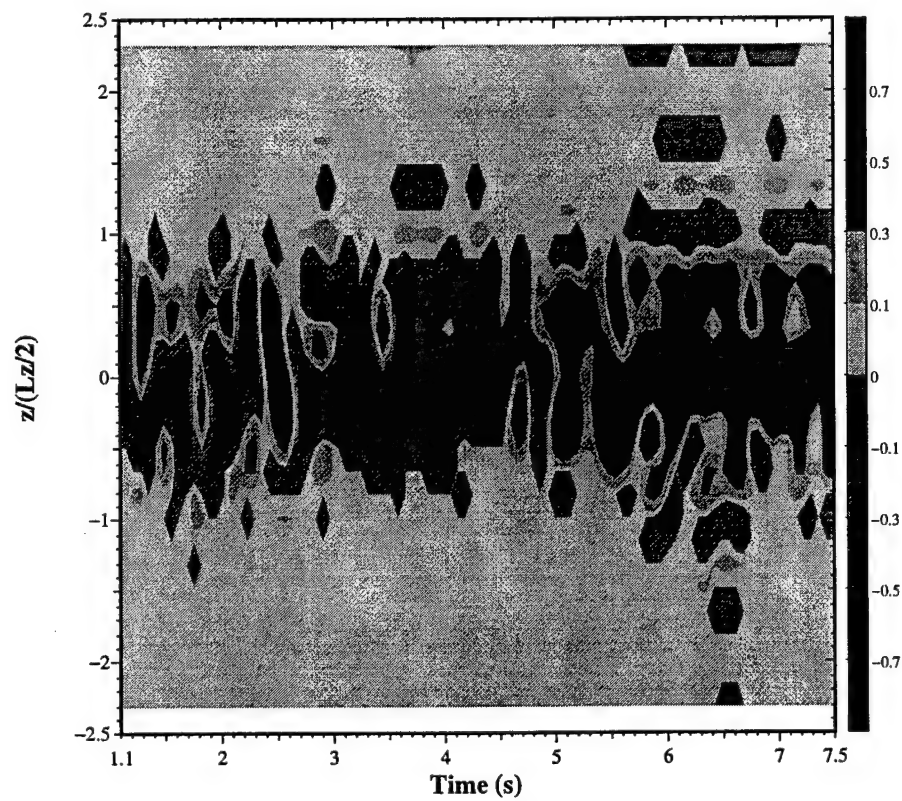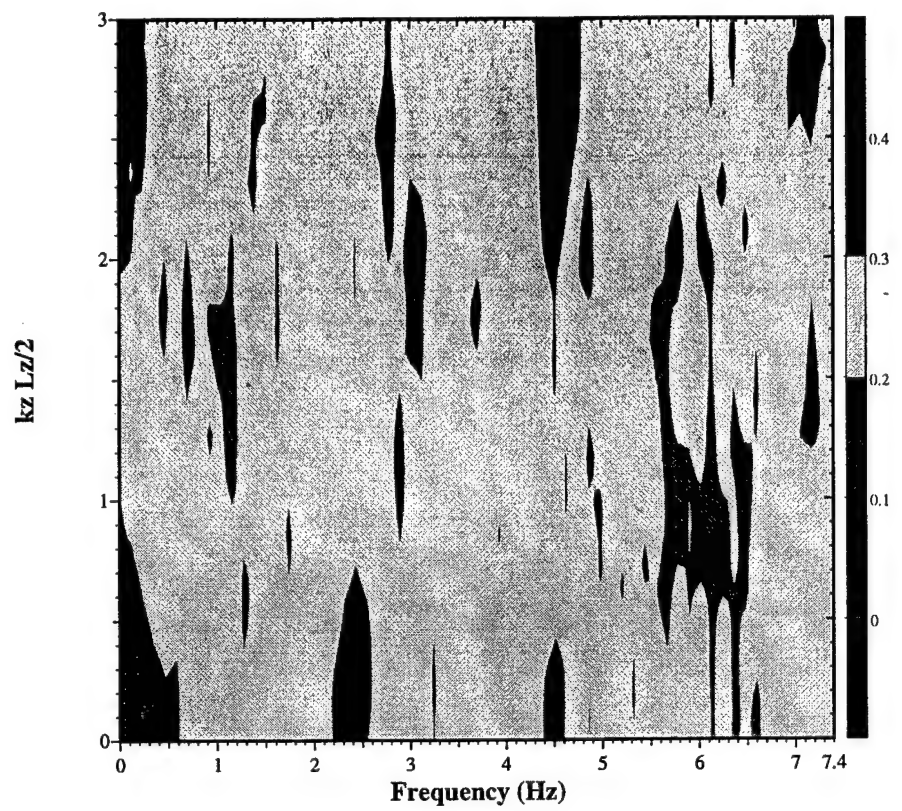
27

Figure 12: Frequency/spanwise wave number spectra (top) and sample time series (bottom) of wall pressure fluctuations in the boundary layer with 3-D mode forcing.

by $\lambda_z/2$.

Without mode forcing, the flow is unstable to background disturbances. The most amplified TS frequency is approximately 38Hz, which is well above our acquisition rate. In the spectra, we observe two narrow peaks at 4.5Hz and 2.5Hz, with $k_z\lambda_{z3-D}/2 = 2.5$ and 0.3, respectively. The spanwise wave lengths in these cases are $0.17\lambda_{z3-D}$ and $1.6\lambda_{z3-D}$. From the pressure time series, the former refers to the small-scale fluctuations seen in the bottom part of Figure 11.

With mode forcing we expect the streamwise vortex mode to produce a quasi-steady feature in the pressure distribution. This can be seen to some degree as the long dark region in the pressure time series in the bottom of Figure 12. When we examine the spectra, we observe a broad peak of intermediate height at $k_z\lambda_{z3-D}/2 = 1$ and 6Hz. This peak was not in the spectra without mode forcing, and on the basis of its spanwise wave length is indicative of the streamwise vortex mode. Further analysis of the pressure data will follow the sections on the development of the actuator array and the use of the 1×7 array of hot-wires.

5 Wall Actuator

This section summarizes the design and testing of the actuator array used in controlling the streamwise vortex mode in the boundary layer. The complete details of the design are contained in the thesis by Peto (1997).

The objectives of the actuator were:

1. To be able to introduce a standing pattern in the wall surface, with a spanwise wave length which is approximately equal to $\lambda_{z3-D}/4$.

2. To have a low-mass design which had a high enough amplitude and frequency response.

3. To have a design which would be controllable by ttl-level voltages produced by the parallel output of a digital computer.

4. To have a design which had a negligible effect on the flow when not being actuated.

5.1 Electro-Magnetic Actuators

To accommodate these objectives, the actuator was designed around an electro-magnetic system similar to that of Ghassemi (1992). This approach uses an array of current-conducting elements actuated by an electro-magnetic force produced by an interaction with an array of high-strength permanent magnets. A schematic diagram is shown in Figure 13. The magnets were custom made of Neodymium-Iron-Boron by Dextor Corp. The magnets were 2.75in in the flow direction, by 3.93in long, by 0.157in (4mm) thick. The poles of the magnets were on the ends of the longest dimension. 16 magnets were grouped into an array as shown in the top-left part of Figure 14. For this, 1mm thick plastic shims were placed between each magnet. This gave a 5mm spacing between the centerlines of the gaps between the magnets. When placed in the tunnel, the centers between the magnets also lined up with optical sensor holes. The 1mm spacing was also important in shaping the magnetic flux lines between the magnets.

The magnets are placed so that the poles alternate between neighbor magnets. This establishes magnetic flux lines which curve from the North to the South poles
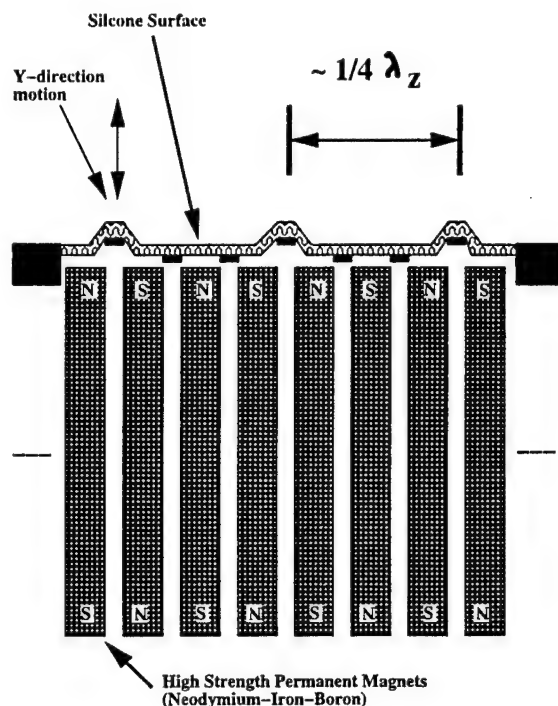
Figure 13: Schematic of wall contouring produced by actuator array.

of adjacent magnets. 2mm wide by 0.051mm thick brass strips overlayed each seam between the magnets. This is shown in the bottom photograph of Figure 14. The strips were formed by a chemical etching process which insured straightness and uniformity of width. The placement of the strips insured that they were centered in the magnetic flux lines between adjacent magnets. When a current was passed through the magnets, the brass strips deflected due to the electro-magnetic force. The direction of the current determined if the deflection was away from or towards the magnet (wall). In the design, an attracting force would pull the strips to lie flat on the magnets.

The brass strips were covered by a thin flexible sheet so that a smooth surface was formed when they were lying on the magnets. This is illustrated in Figure 13. The thin sheet was a medical grade elastomer which had excellent properties
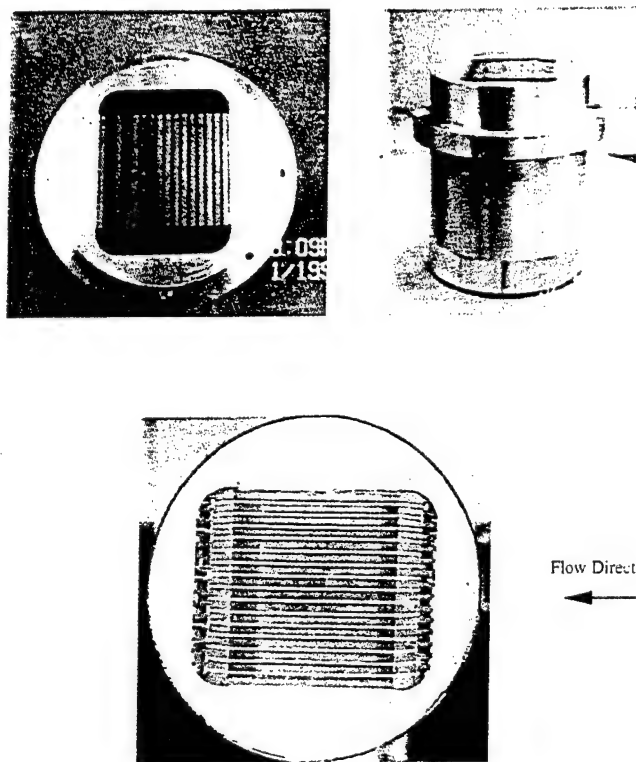
31

Figure 14: Photographs of wall actuator array.

such as elasticity and strength. The sheet had a uniform thickness of 0.178mm. The elastic sheet was bonded around the perimeter of the disk holding the actuator array (Figure 14). In addition, it was bonded to the top surface of each of the brass strips. The latter assured that the strips would hold the sheet down when the strips were being held by a downward magnetic force. This was especially important when excitation of a particular spanwise wave length required an actuator to be extended from the wall while its neighbor was held flat against the wall. Figure 13 illustrates such as condition.

5.2   Actuator Control Circuitry

The function of the control circuitry was to provide voltages and currents necessary to actuate the individual elements from a ttl-compatible signal provided by a digital computer parallel output. A schematic of the circuit used to control this task is shown in Figure 15. This represents one of 15 identical circuits. The circuit provides positive isolation through an optical interface. In addition it allows adjustments for a gain and offset of the computer input. In operation, a logical 0 from the computer was set to provide a -3V output. This provided a wall-ward force which held the actuator strip on the top surface of the magnets. When a logical 1 was sent by the computer, the gain was set to provide a +10V output which deflected the actuator strip away from the wall. The final amplifier stage is base on a high-power operational amplifier which can provide output currents of up to 5A. At the largest amplification setting, the actuator strips would deflect approximately 2mm from the wall. For the wind tunnel conditions used, this corresponded to approximately 20% of the boundary layer thickness. The circuit settings were adjusted so that the
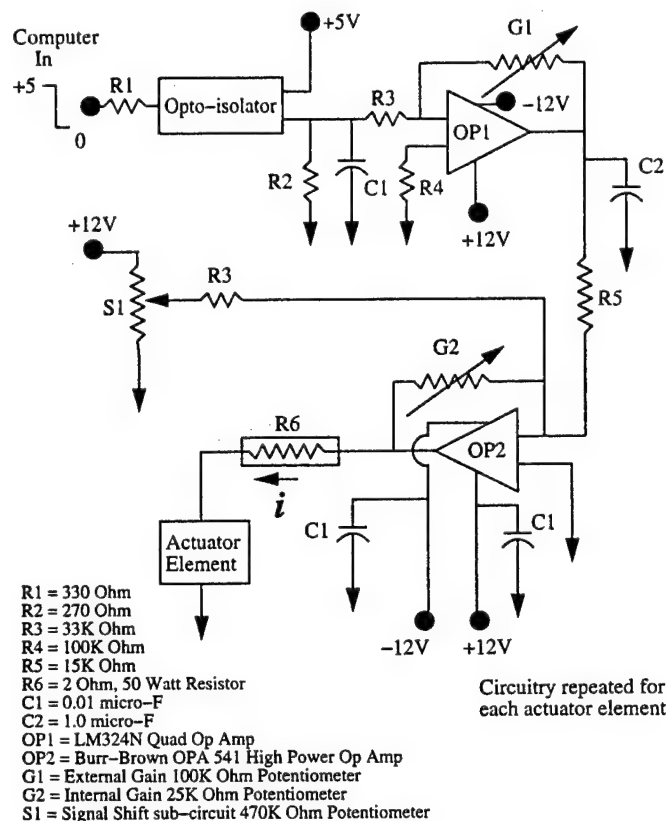
Computer
In
+5

R1

+5

0

Opto-isolator

+5V

G1

OP1

−12V

R3

R2

C1

R4

+12V

C2

+12V

S1

R3

R5

G2

R6

OP2

i

Actuator
Element

C1

C1

−12V

+12V

R1 = 330 Ohm
R2 = 270 Ohm
R3 = 33K Ohm
R4 = 100K Ohm
R5 = 15K Ohm
R6 = 2 Ohm, 50 Watt Resistor
C1 = 0.01 micro-F
C2 = 1.0 micro-F
OP1 = LM324N Quad Op Amp
OP2 = Burr-Brown OPA 541 High Power Op Amp
G1 = External Gain 100K Ohm Potentiometer
G2 = Internal Gain 25K Ohm Potentiometer
S1 = Signal Shift sub-circuit 470K Ohm Potentiometer

Circuitry repeated for
each actuator element

Figure 15: Schematic of one channel of actuator control circuitry.

same displacement was produced in each strip for the same output from the computer. The effect of different deflection amplitudes on the flow will be presented in a later section.

5.3 Actuator Response

Tests were conducted to determine the actuator amplitude and frequency response characteristics. This was done by placing a hot-wire over one of the actuator strips. A sinusoid was then input to that channel of the control circuit to drive the actuator in a periodic motion. This was done without flow. The voltage from the hot-wire, proportional to the wall-normal velocity component, was digitally acquired. To determine the frequency response, an frequency of the sine wave input
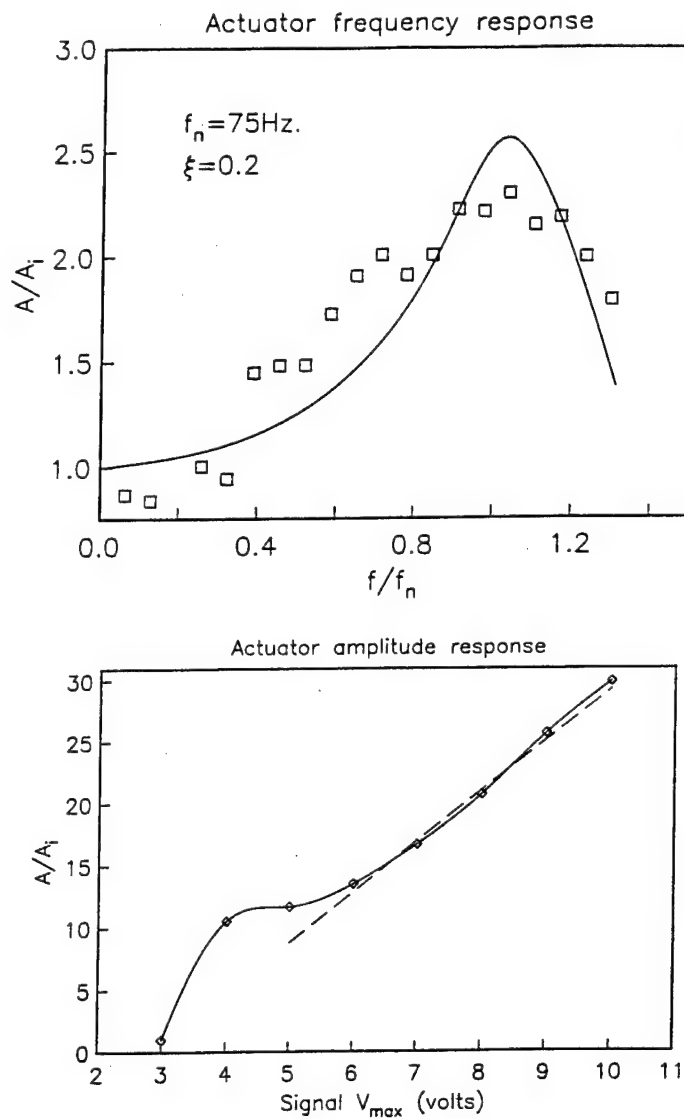
Figure 16: Frequency and amplitude response of the actuator array.

to the actuator was varied while keeping a fixed amplitude. The result is shown in the top of Figure 16. The symbols refer to the measurements. We expect the actuator to behave as a 2nd order system (spring- mass-dashpod). The solid curve represents a second order response with a natural frequency of 75Hz and a damping factor of 0.2. This response is quite suitable for our application since we intend to introduce quasi-steady motions of the wall with frequencies below $f/f_n = 0.4$. In this range, the frequency response is nearly flat (constant).

35

An amplitude calibration of the actuator was performed by varying the amplitude of the sine input at a fixed frequency below $f/f_n = 0.4$. The result is shown in the bottom part of Figure 16. This shows that there was an input voltage above 5V with which there was a linear input-output relationship. Below that, there was some overshoot in the response. For this reason, only amplitudes which were within the linear region, corresponded to settings of 45% or larger of the full scale, were used.

6   Wall-velocity Array

A rake of 7 hot-wire probes were constructed in order to document the effect of the actuator as well as to compare to the results from the optical pressure sensor array. A special insert was constructed which held the sensors in one of the circular openings in the back wall which otherwise accepted the optical pressure or actuator arrays. A schematic is shown in Figure 17. Holes were drilled in the insert to allow the body of the probes to pass through from the back to the measurement side of the wall. Set screws secured the probes from moving.

The spanwise spacing of the hot-wires was 5mm. This allowed them to line up with the actuator strips and holes in the optical sensor. The distance of the sensors from the wall was set so that they were within the linear mean profile region ($U/U_o \leq 0.4$). The height of all the sensors was set to be the same.

The hot-wires were powered by 7 constant temperature anemometers. The voltages from these were digitally acquired and converted into velocities using a 4th order polynomial with coefficients which were determined by previous calibration.
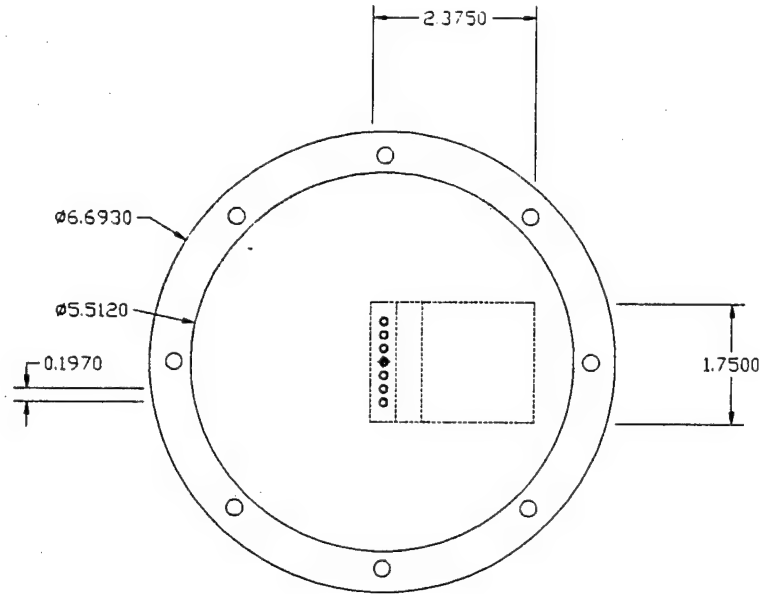
Figure 17: Top-view schematic of 7×1 hot-wire array plate.

6.1 Wall-velocity Measurements

The experimental conditions were the same as those used by Corke and Gruber (1996). For these, the basic flow was a Falkner-Skan boundary layer with the pressure gradient parameter, $\beta = -0.06$. The unsteady initial conditions provided by an array of heating wires located upstream excited a plane TS mode at 38Hz, and pairs of oblique modes with wave angles of 59° and a frequency of 19Hz. This led to the resonant growth of the oblique modes with a spanwise wave length of 60.5mm.

The top part of Figure 18 shows the relative location of the actuator array and the array of hot-wires with respect to the growth in amplitude of the oblique modes. Both are located in the nonlinear region where the amplitude of the subharmonic oblique modes is large. The bottom part of Figure 18 shows the spanwise distribution in the amplitude of the oblique (19Hz) mode. This shows the amplitude
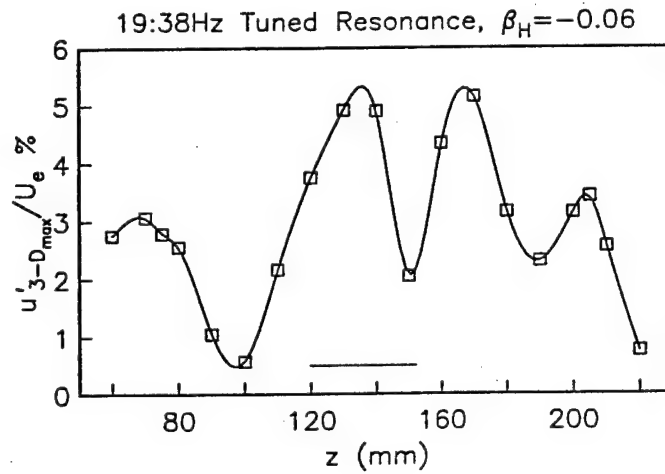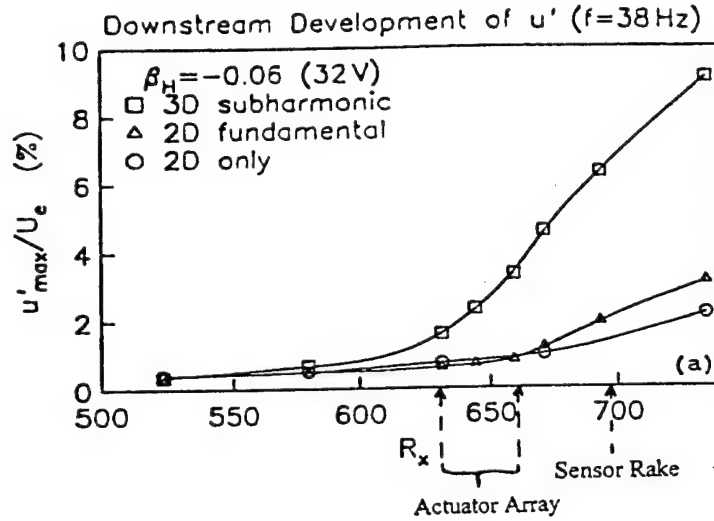
37

Figure 18: Streamwise position of the actuator and hot-wire arrays with respect to the amplitude of the 3-D mode (top) and the spanwise scale and location of the sensor array (line, bottom plot) with respect to 3-D spanwise amplitude distribution.
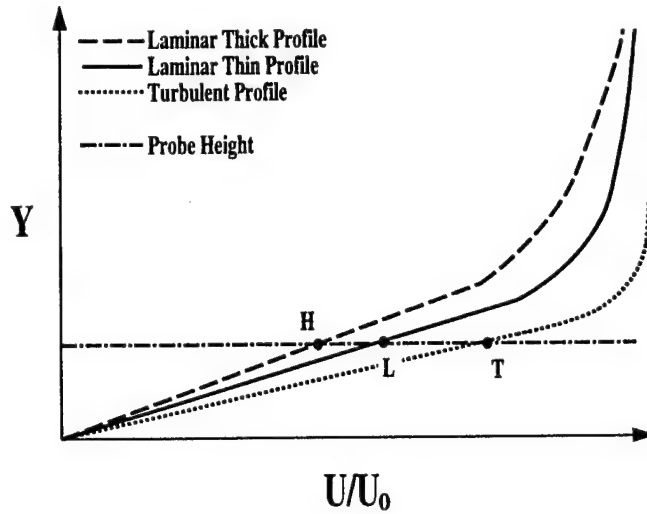
38

Figure 19: Schematic drawing of idealized mean boundary layer profiles and the hot-wire sensor height.

maxima and minima which are associated with the 3-D mode. The spacing between the minima corresponds to $\lambda_{z_{3-D}}/2$. The growth of the oblique modes produces new modes as a result of nonlinear interactions. The one of most interest is the streamwise vortex mode. This has a spanwise wave length of $\lambda_{z_{3-D}}/2$. The horizontal line located at $120\text{mm} \leq z \leq 155\text{mm}$ marks the location and spanwise extent of the hot-wire array. These 7 sensors also line up with the seven actuators in the center of the array, numbered 5 to 11, respectively.

The hot-wires were placed close to the wall, in the linear profile region. This is exemplified in the schematic in Figure 19. This shows three possible mean velocity profiles that the hot-wires could encounter. Two of these are laminar profiles with different thicknesses. Such a variation in the boundary layer thickness occurs in the spanwise direction as a result of the streamwise vortex mode. In these instances, a sensor at a fixed height above the wall would measure a variation in the mean velocity which was consistent with variations in the boundary layer thickness, eg.,

39

lower or higher mean values for thicker or thinner boundary layers, respectively. An additional condition is if the flow were turbulent. In this case, the wall shear stress would increase, so that a sensor at a fixed height above the wall would measure a large increase in the velocity.

We used this general behavior of the mean flow as an indicator of the spanwise structure and general state of the flow for different actuator conditions. A total of 42 experiments were performed with various combinations of actuators operated with different amplitudes and oscillating frequencies (including d.c.). All these cases are contained in the thesis by Peto (1997). Some of the results are included in the following.

6.1.1 Amplitude Effect: Single Actuator

Part of the series of experiments were designed to determine the optimum wall deflection needed to produce a response in the flow. A sample of this is shown in Figure 20. This corresponds to operating a single actuator strip which was located at the spanwise position of the 3-D mode amplitude maximum. The top plot shows the normalized deviation of the mean velocity as a function of the actuator amplitude. This also corresponds to the spanwise location where the boundary layer is thickest. The bottom shows the amplitude of the total rms of the velocity fluctuations measured by the sensor. The solid and long-dashed curves correspond to a d.c. displacement of the actuator strip. The short-dashed curve corresponds to oscillating the strip at a near 3-D mode frequency of 18Hz.

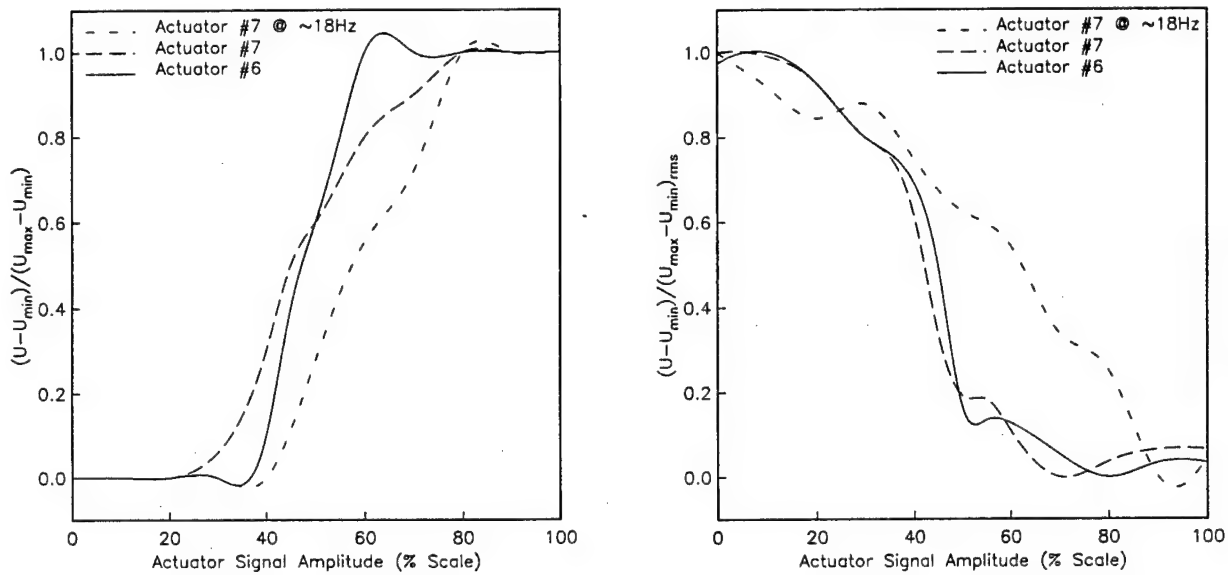In terms of the mean velocity, there was a minimum amplitude below which the

Figure 20: Effect of raising a single actuator strip near the 3-D mode amplitude maximum on the mean velocity (left) and the r.m.s velocity (right).

actuator had no significant effect. Similarly, there was a maximum amplitude above which further increases had no effect. The precise amplitude limits were somewhat dependent on if it was a d.c. or fluctuating motion, and the location of the actuator with respect to the spanwise amplitude maximum.

A similar picture was found on the basis of the total rms values. This is seen in the bottom part of Figure 20. With the lower actuator amplitudes, there begins a gentle decrease in the rms fluctuations. At approximately 40% of full-scale, we observe a sharp decrease in the fluctuation amplitude. This flattens out for amplitudes above approximately 60%. As with the results in the top plot, the oscillating actuator has a more gradual effect on the flow response with changing amplitude. These results were instrumental in choosing the amplitudes when more than a single actuator was use.

41

6.1.2 Multiple Actuators

The rake of hot-wire sensors was used to evaluate the effect of different actuator conditions. Here we were looking at the content of the velocity fluctuations as well as the mean velocity value in the context of the classification illustrated in Figure 19. Figure 21 shows an example of the data from the hot-wire array. This shows a segment of the time series from each sensor (solid curve), the mean velocity value at that spanwise location (long-dashed line), and the spanwise-averaged mean velocity value (short-dashed line). Note that the velocity at the short-dashed line does not change between the plots. The case shown in Figure 21 corresponds to the base flow with oblique mode forcing but no actuation. Examining this figure we observe many of the fundamental characteristics. For example, the top trace corresponds to the spanwise location where the amplitude of the oblique modes are a minimum. The period of the fluctuations corresponds to the fundamental frequency. In contrast, the bottom traces correspond to the spanwise location where the oblique mode amplitude is a maximum. In terms of the mean velocity, the higher local values at the bottom positions indicates that the boundary layer is locally thicker compared to the upper portion.

Alternatively we found it useful to examine 1-D spectra of velocity fluctuations from each of the sensors. The spectra for the conditions of Figure 21 are shown in Figure 22. This is shown as a 3-D perspective plot with frequency on horizontal axis, the spanwise position in terms of the actuator number on the depth axis, and the normalized spectral amplitude, $u_{rms}(f)/U_\infty$, on the vertical axis. Note that in order to better show spectral peaks, the view-point has been rotated so that the
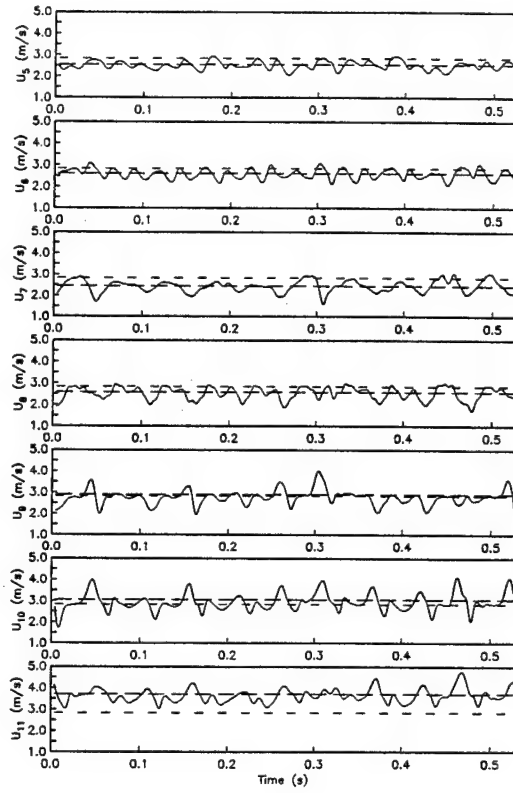
42

Figure 21: Velocity time series for 7×1 hot-wire array for case with 3-D mode forcing, but no actuation.
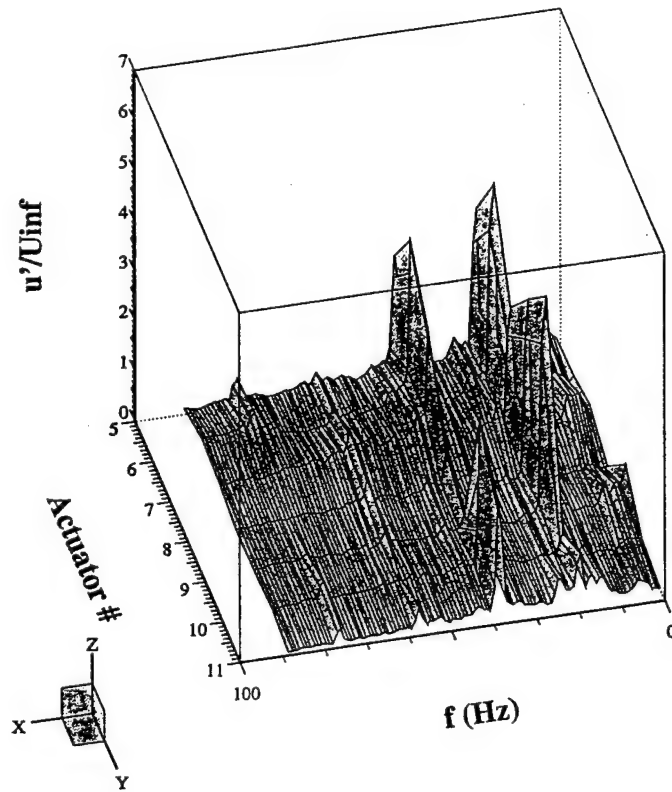
Figure 22: Spectra from 7×1 hot-wire array for case with 3-D mode forcing, but no actuation.

highest frequency is at the left.

The spectra show many of the basic characteristics of the subharmonic 3-D mode transition. These include the spanwise amplitude variations of the subharmonic (19Hz) and fundamental modes (38Hz), with the latter having a spanwise wave length which is one-half that of the subharmonic. The spanwise variation of the mean flow (d.c.) which is associated with the streamwise vortex mode is not as apparent in these series of 1-D spectra. Later analysis of the time series using 2-D spectral estimates is needed to bring out this feature.

The results from a series of actuator conditions taken from figures like these are summarized in Figures 23 to 25. These show the normalized change in the mean velocity at each spanwise location as a result of different actuator conditions. In these plots, the quantity U_{ind} refers to a velocity "indicator function" which is the value of the mean velocity at the fixed height above the wall for a given actuator condition. The quantity $U_{control}$ refers to the mean velocity value with no actuator motion. Note that $U_{control}$ is a function of the spanwise location which reflects the streamwise vortex mode which causes the boundary layer to be thicker at the spanwise location of actuator 5 and thinner at actuator 11. The difference between these two indicates the change produced by the actuation. Generally a higher velocity means a thinner, more stable, boundary layer. Therefore, a positive value of $U_{ind} - U_{control}$ is desirable from a control aspect.

With this in mind, Figure 23 shows the effect of three different d.c. amplitudes of actuator 7 on the flow. Actuator 7 is near the spanwise location of an amplitude **maxima** in the 3-D mode at the fundamental frequency (38Hz). This mode has
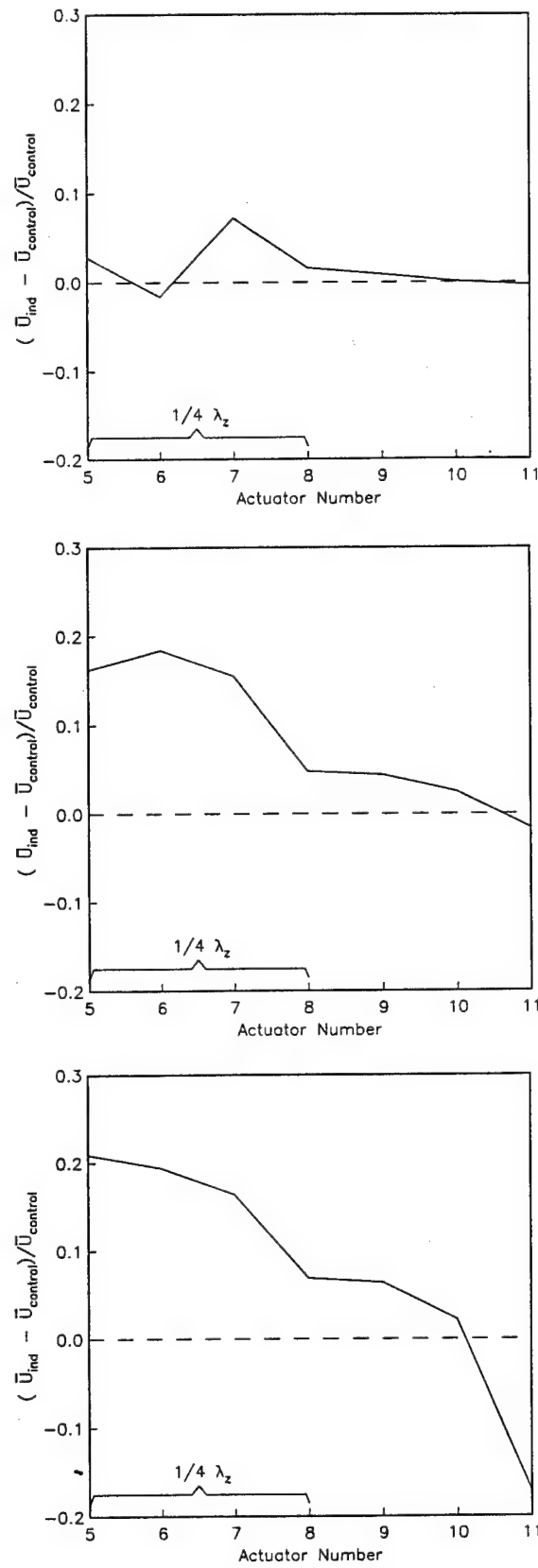
45

Figure 23: Change in the local mean velocity indicator while deflecting actuator number 7 by 30% (top), 45% (middle) and 100% (bottom).

the same spanwise wave length as the streamwise vortex mode. At the minimum useful amplitude (top) of 30% based on Figure 20, we observe a spanwise-localized thinning of the boundary layer. At a slightly higher amplitude of 45% (middle), a greater thinning of the boundary layer occurs, which is distributed over a larger spanwise region. Increasing the amplitude to 100% (bottom) gives only a small additional improvement, and has a negative impact near actuator 11.

Figure 24 demonstrates that the positive effect of a single actuator element is dependent on its spanwise location with respect to the streamwise vortex mode. This shows the result for 100% d.c. amplitude of actuator 9 (top) and actuator 11 (bottom). Actuator 9 is located near the amplitude **minima** in the 3-D mode at the fundamental frequency (38Hz). At this location, the actuator has a minimal effect. Like actuator 7, actuator 11 is located at the next amplitude **maxima** in the 3-D mode at the fundamental frequency. As a result it has a substantial positive effect which is fairly similar to actuator 7 (bottom, Figure 22).

The spacing and number of actuator strips was designed to provide the a range of spanwise wave lengths which was compatible with the generated streamwise vortex mode. In Figure 25, an actuator arrangement which reinforces that wave length was investigated. In this case, elements 5, 8 and 11 were activated. The top two plots correspond to d.c. amplitudes of 40% and 90%. The bottom plot corresponds to a periodic actuator motion with a peak amplitude of 100%.

For the two cases with a d.c. amplitude, the actuators have a positive effect on the boundary layer. At the higher amplitude, the we observed the largest magnitude of thinning compared to any of the other cases. However, when the elements
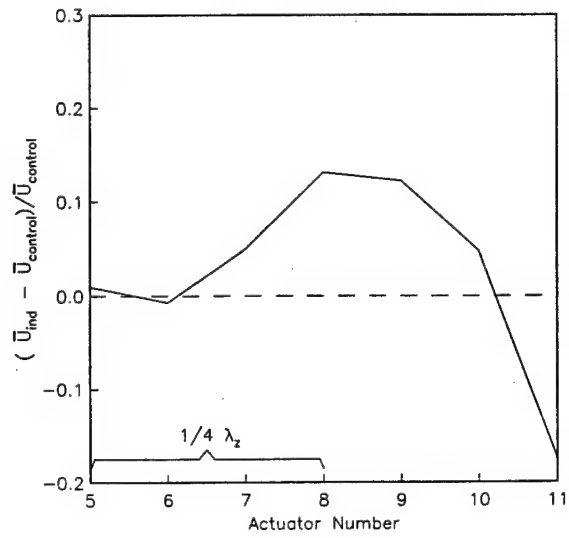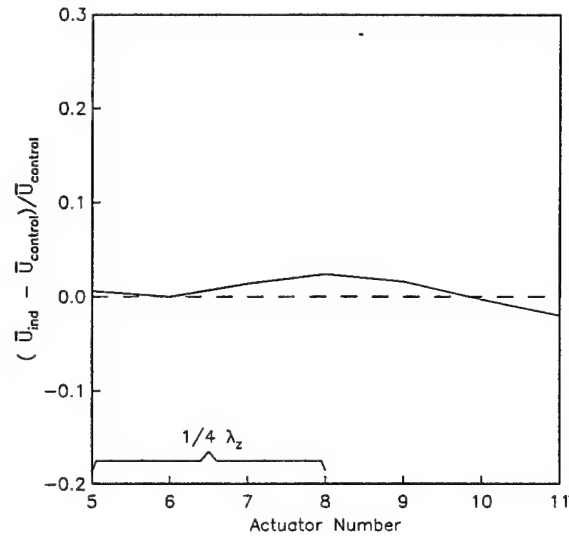
47

Figure 24: Change in the local mean velocity indicator while deflecting actuator number 9 (top) or 11 (bottom) by 100%. .
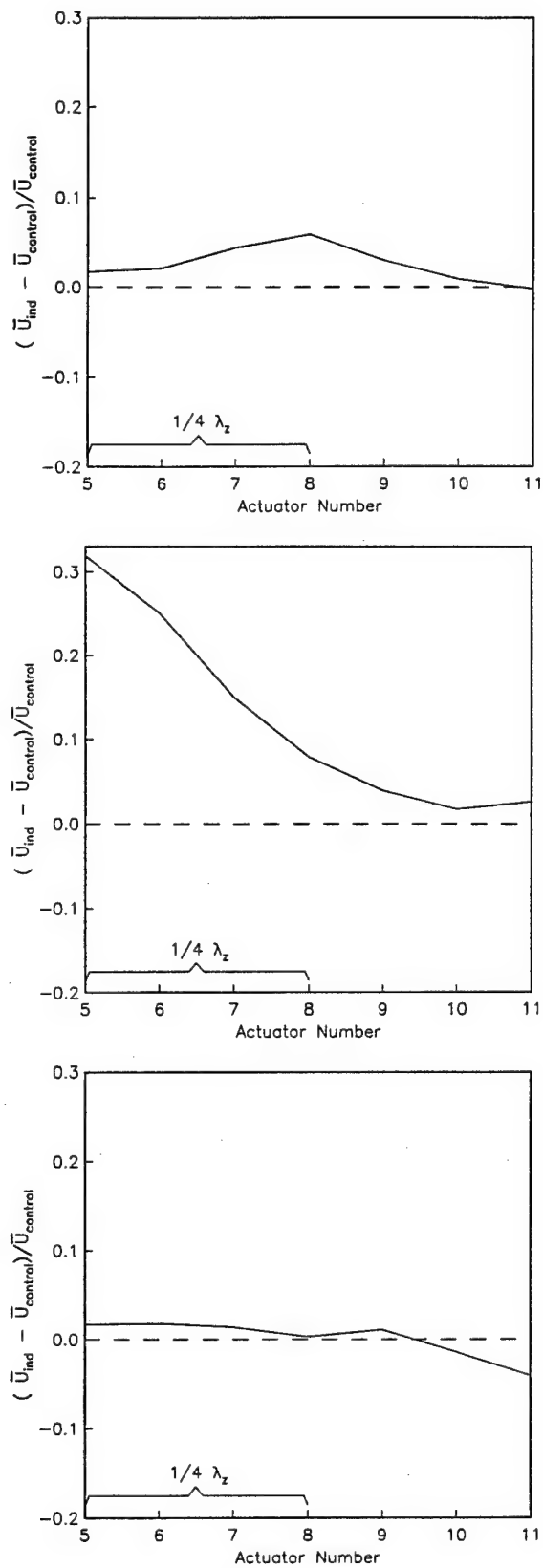
Figure 25: Change in the local mean velocity indicator while deflecting actuator numbers 5,8,&11 at 45% (top) and 90% (middle) of full scale, and when oscillating at 17.75Hz at 90% of full scale (bottom).

49

were oscillated, there was almost no net change in the mean velocity. This was a general result which was found regardless of the actuator combinations tested. It is important to point out that from an energy point of view, a lower input power is required to oscillate the actuator elements at the same peak amplitude used for the d.c. input. We chose a frequency which was close to the 3-D mode frequency in an attempt to interfere with its nonlinear development. The spectra indicated that this indeed occurred, however, little net effect was observed on the mean flow. We deduced from this that there was only a minor effect on the streamwise vortex mode, and from that point of view, was not as effective as a static deflection of the wall.

7   2-D Spectral Analysis

Software was developed to perform 2-D spectral analysis of the hot-wire array space-time series, and the data series from the optical pressure sensor. Details of this aspect of the work are contained in the thesis by Speer (1997), and was supported by the ASSERT award which complimented this research. A further summary of the software development and results are included in the Final Report for the ASSERT Research.

The software was designed to perform 2-D filtering on the data series from the two different sensor arrays as well as calculate 2-D (frequency/spanwise wave number) spectra. These were analyzed to assess the effectiveness of the different actuator conditions examined by Peto (1997) and previously described above. Some of the complimentary results of this analysis are presented here in the context of
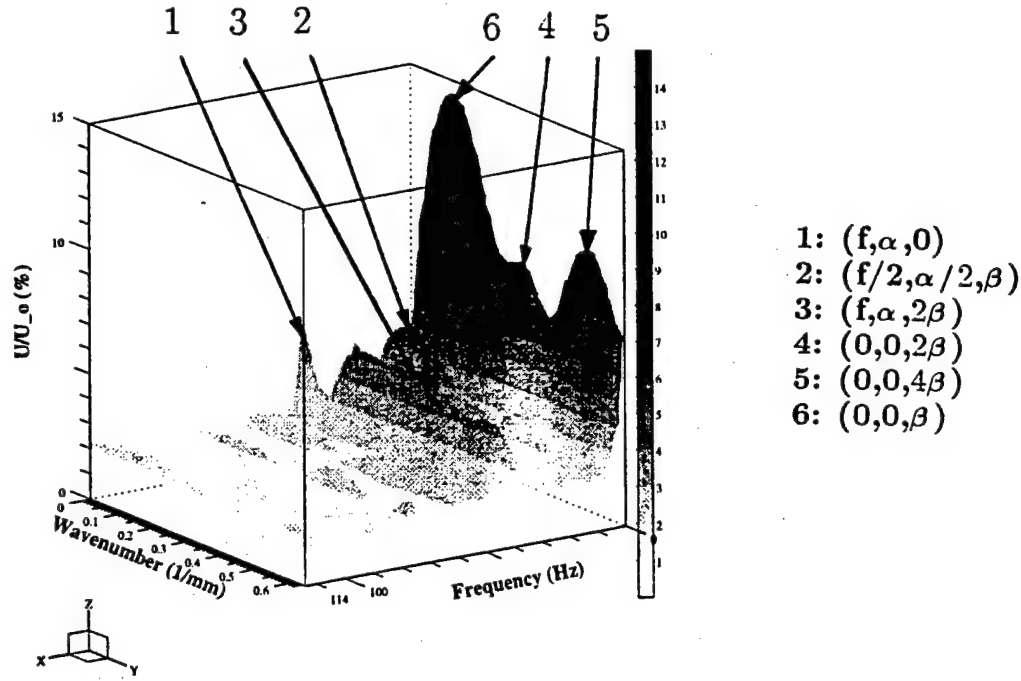
Figure 26: Frequency/wave number spectra of velocity from 1×7 hot-wire array with mode forcing but no actuation.

the actuator effectiveness.

The processing consisted of transforming the 2-D data sets consisting of the simultaneous time series from the 1×7 spatial array of hot-wire sensors or pressure sensors into the frequency domain using a 2-D fast-Fourier-transform (FFT). This data was then either low-pass filtered to reconstruct the data to a finer spatial resolution and enhance features associated with the streamwise vortex mode, or used in the calculation of ensemble-averaged 2-D auto-spectra. The spectra were further analyzed to identify energy in specific modes to determine the effectiveness of actuator configurations. In contrast to the 1-D spectra presented in a spatial format in Figure 21, the 2-D spectra were able to identify zero frequency modes, such as the streamwise vortex mode, because of their periodic spanwise component.

An example of the 2-D spectrum for the same conditions in Figure 21 is shown in

51

Figure 26. This is shown in a 3-D perspective view with frequency on the horizontal axis, wave number on the depth axis, and amplitude on the vertical axis. The conditions correspond to the boundary layer with oblique mode forcing, but without actuation. The spectrum clearly shows peaks which we can identify as the initial and nonlinear modes. The principle ones have been numbered 1 to 6 and are listed in a (frequency, streamwise wave number, spanwise wave number) format on the right side of the plot. The peak associated with the initial oblique mode pair is labeled 2. The 3-D mode produced by a nonlinear interaction which is at the fundamental frequency and twice the spanwise wave length, is labeled as peak 3. Both these modes are traveling (nonzero frequency) and were identified in the 1-D spectra such as in Figure 21.

The peak labeled 4, corresponds to the streamwise vortex mode, which we are primarily trying to affect by the actuators. It has zero frequency and a spanwise wave number which is twice that (one-half the spanwise wave length) of the initial 3-D mode.

Because the 2-D spectra are able to identify the energy in the spanwise-stationary modes such as the streamwise vortex mode, they are an excellent tool to assess the effectiveness of the different actuator configurations. For example, Figure 27 shows the effect of single actuator number 7 at three deflections. This can be directly compared to Figure 23. There are a number of details that can be pointed out in the spectra, however just focusing on the zero frequency modes, we observe significant differences. Recall that actuator 7 is located near the spanwise location of the 3-D mode amplitude maximum. When the actuator is at 30% amplitude (top

plot), we actually observe a slight increase in the amplitude of the streamwise vortex mode (peak 4). Increasing the amplitude to 45% (middle plot) we observe a further increase in the amplitude of peak 4. Finally at a 90% displacement amplitude of actuator 7, the levels of all the zero frequency modes decrease.

More detail of the results from the 2-D spectra are included in the Final Report for the AASERT Grant. The remainder will now focus on the results obtained from the optical pressure array.

8   Pressure Sensor Results

As described earlier, detailed analysis of the boundary layer with mode forcing and actuation was done using a 1×7 subset of the 15×15 optical pressure array. That subset was shown in Figure 10. The 1×7 array was located at the same streamwise and spanwise position as the 1×7 hot-wire array (the sensor plugs were exchanged). Therefore they were in the same relative position to the actuator array. The spanwise spacing between individual diaphragms was the same as the spacing between the hot-wires so that they had the same resolution and encompassed the same space in the flow.

Sample time series of the pressure fluctuations measured by the 1×7 pressure array were presented in Figures 11 and 12. Figure 12 in particular corresponded to the case with mode forcing. The pressure measurements are intended to focus on low frequency modes. The predominant ones are the zero frequency modes in the spectrum of Figure 26 which have a spanwise wave length of 1, 0.5 and $0.25\lambda_{z3-D}$. These correspond respectively to peaks 6, 4 and 5 in Figure 26. In terms of the
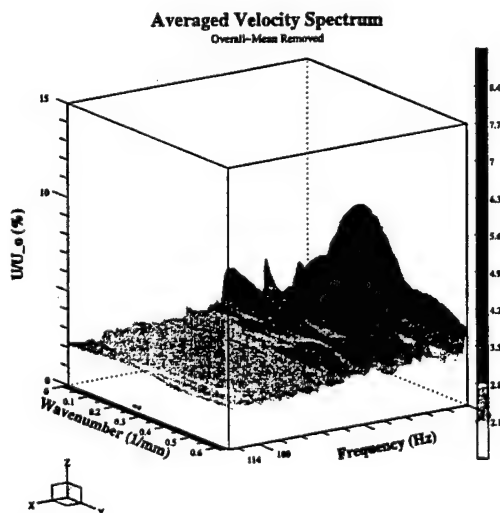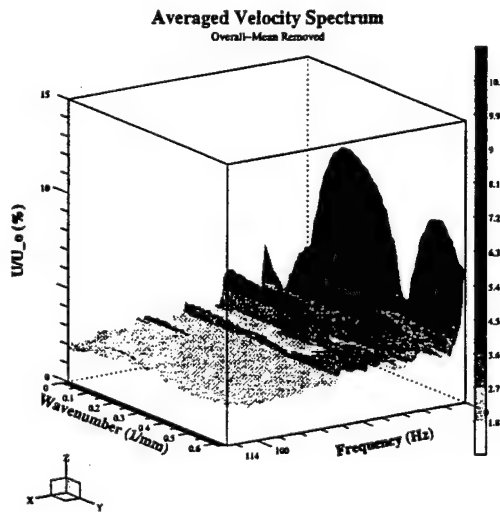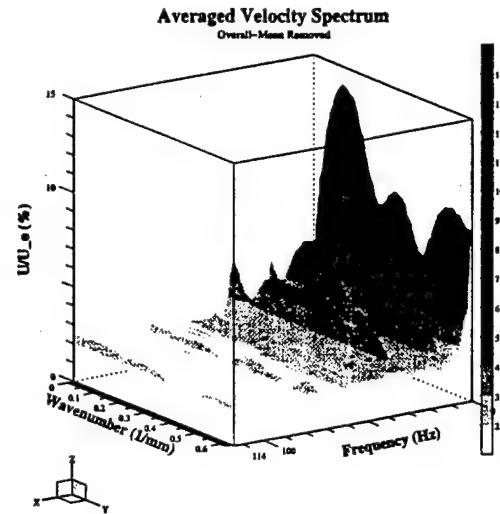
Figure 27: Frequency/wave number spectra of velocity from 1×7 hot-wire array with actuator 7 at 30% (top), 45% (middle) and 100% (bottom) deflections.

54

dimensionless wave number, $k_z\lambda_z/2$, these respectively correspond to values of 0.5, 1 and 2. Therefore in the 2-D spectra of the pressure fluctuations, we are looking at peaks which fall along horizontal lines corresponding to $k_z\lambda_z/2 = 0.5$, 1 and 2. Of these three, a peak at $k_z\lambda_z/2 = 1$ would be indicative of the streamwise vortex mode. In the case with mode forcing alone (Figure 12), we observed a peak at $k_z\lambda_z/2 = 1$ at a approximately 6Hz which was not present in the base case without mode forcing.

The following results from the optical pressure sensor will show the effects of a few of the actuator cases corresponding to single actuators numbers 7 or 9 at their maximum deflection, and actuators 5, 8 & 11 at deflection amplitudes of 50 and 90%. The hot-wire measurements indicated (Figure 20, left; Figure 23 bottom) that actuator 7 at this amplitude was effective in thinning the boundary layer (making it more stable). The pressure time series in Figure 28 indicate a similar effect. There we observe the dark-shaded features, indicative of lower pressures than the mean, which are longer in the streamwise extent compared to the Figure 12. In Figure 12, the features with a long streamwise extent had pressures which were alternating in sign. This is statistically born out by comparing the 2-D spectra between Figure 28 and 12. When actuator 7 is elevated, the spectra reveals more energy in frequencies close to d.c., especially with spanwise wave lengths centered near λ_{z3-D} $(k_z\lambda_z/2 = 0.5$.

Figure 29 shows the pressure field when actuator 9 was fully elevated. The hot-wire data indicated (Figure 24 top) that this actuator by itself was not as effective. The pressure field does not appear to support this, where we observe a large region
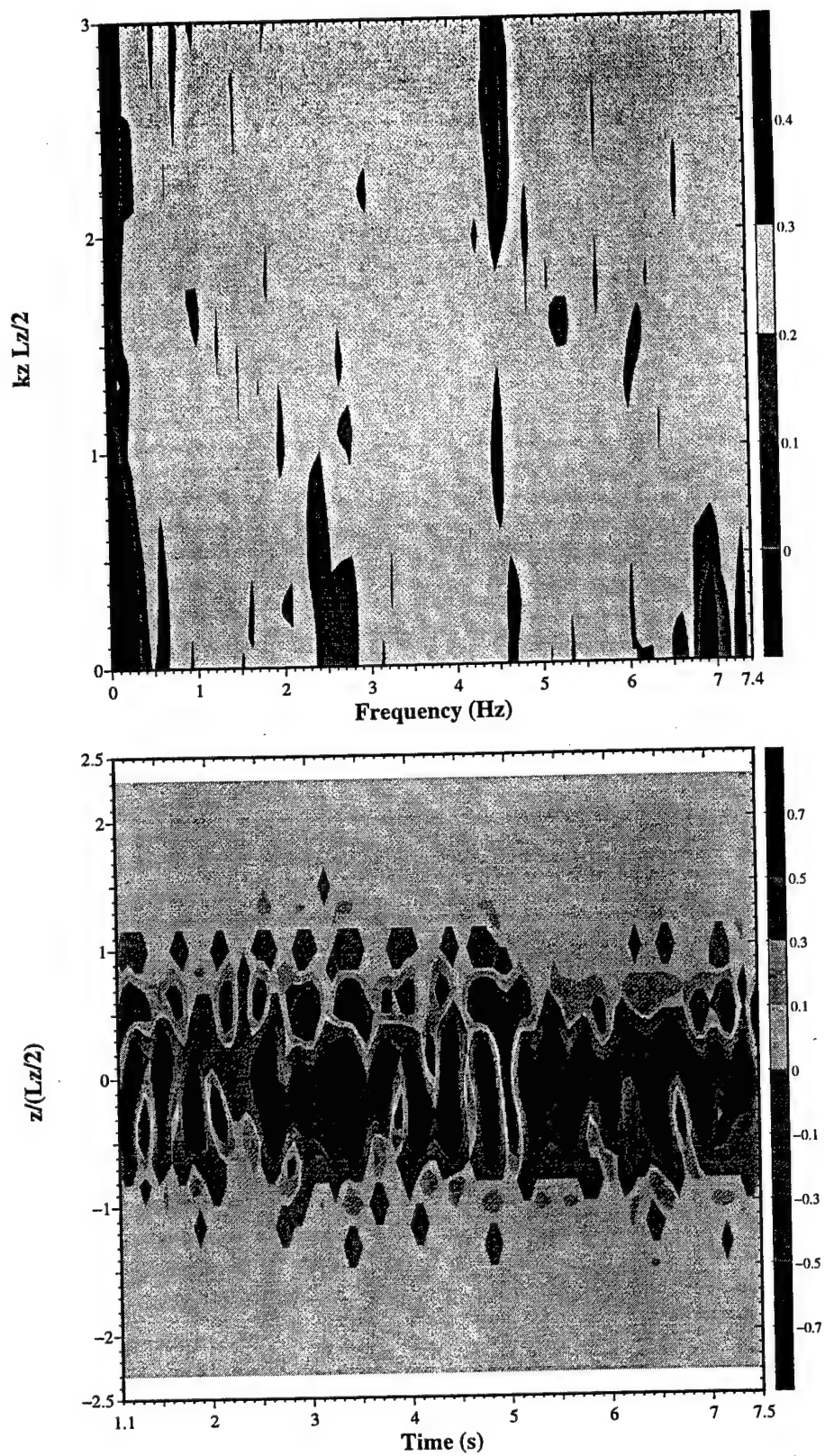
Figure 28: Frequency/spanwise wave number spectra (top) and sample time series (bottom) of wall pressure fluctuations in the boundary layer with 3-D mode forcing and actuator 7 at 90%.
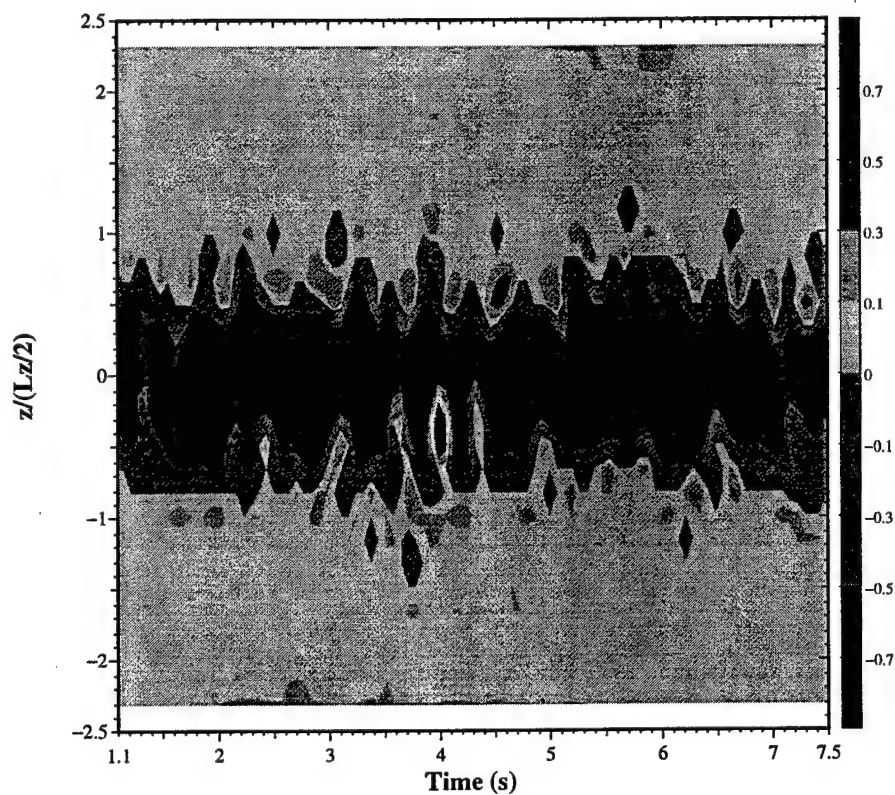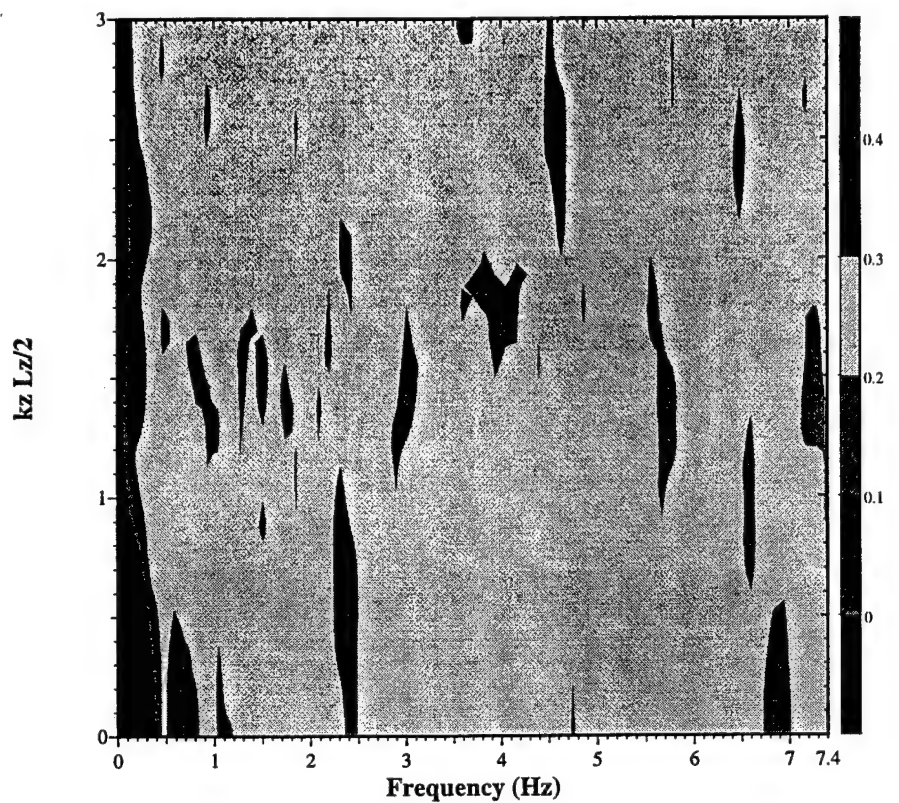
Figure 29: Frequency/spanwise wave number spectra (top) and sample time series (bottom) of wall pressure fluctuations in the boundary layer with 3-D mode forcing and actuator 9 at 90%.

in the flow direction where the pressure is low (dark-shaded). The spectra shows a large peak at d.c. and spanwise wavelength near λ_{z_3-D}.

The remainder figures look at the outcome on the pressure field with two different static deflections of actuators 5,8 & 11. The result with these actuators at 50% amplitude is shown in Figure 30. Here we obtain a consistent picture with the hot-wire results, whereby we see only a minor difference compared to the case without actuation (Figure 12). However when the three actuators are elevated to the maximum, we observe a significant positive effect. This involves the formation of a region (dark-shaded) of low pressure which extends in the flow direction. The spectra reveals that a significant portion of the energy is now at spanwise wave lengths corresponding to λ_{z_3-D} and $\lambda_{z_3-D}/4$. The latter spanwise wave length corresponds to the spacing between the raised actuators.

9 Summary

The research program achieved a number of its initial objectives. These included:

1. The development of the optical pressure sensor, including a neural network approach to categorize the Moire fringe number into pressures.

2. The development of the array of low mass wall actuators.

3. The proper identification of different modes in the transitional boundary layer using the pressure sensor and an array of hot-wires, including the streamwise vortex mode.
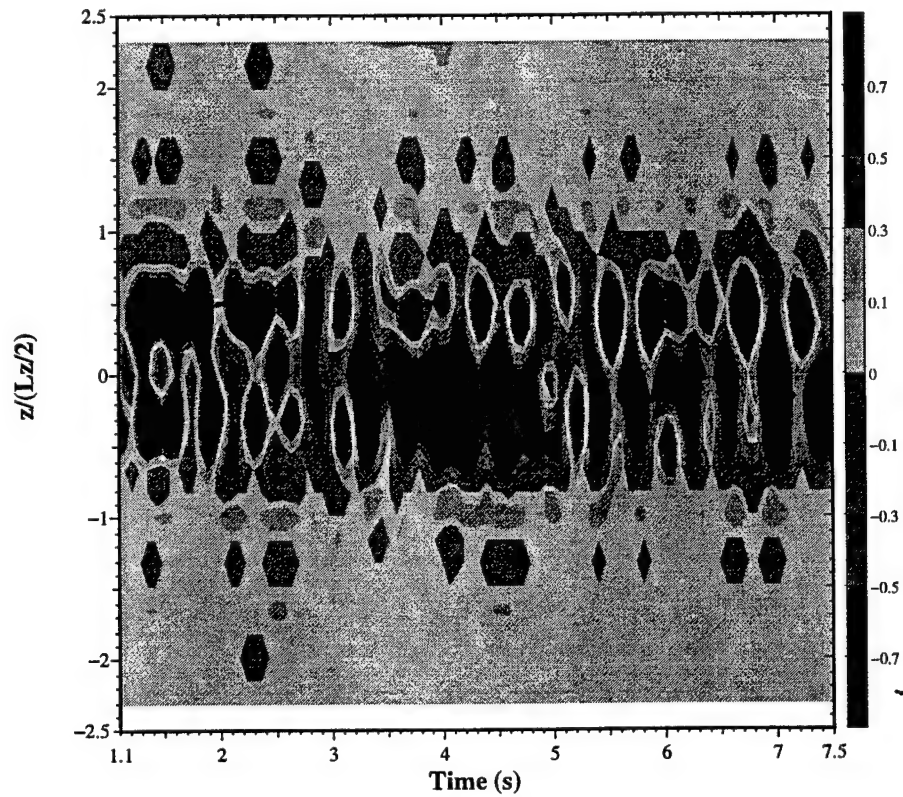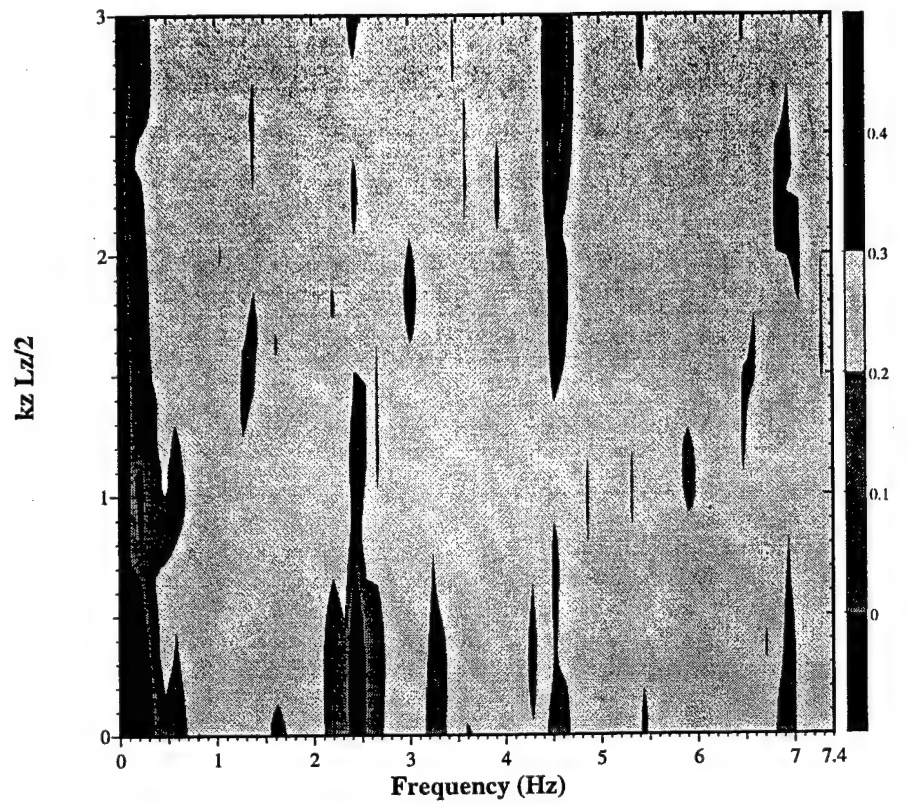
Figure 30: Frequency/spanwise wave number spectra (top) and sample time series (bottom) of wall pressure fluctuations in the boundary layer with 3-D mode forcing and actuators 5,8 & 11 at 45%.
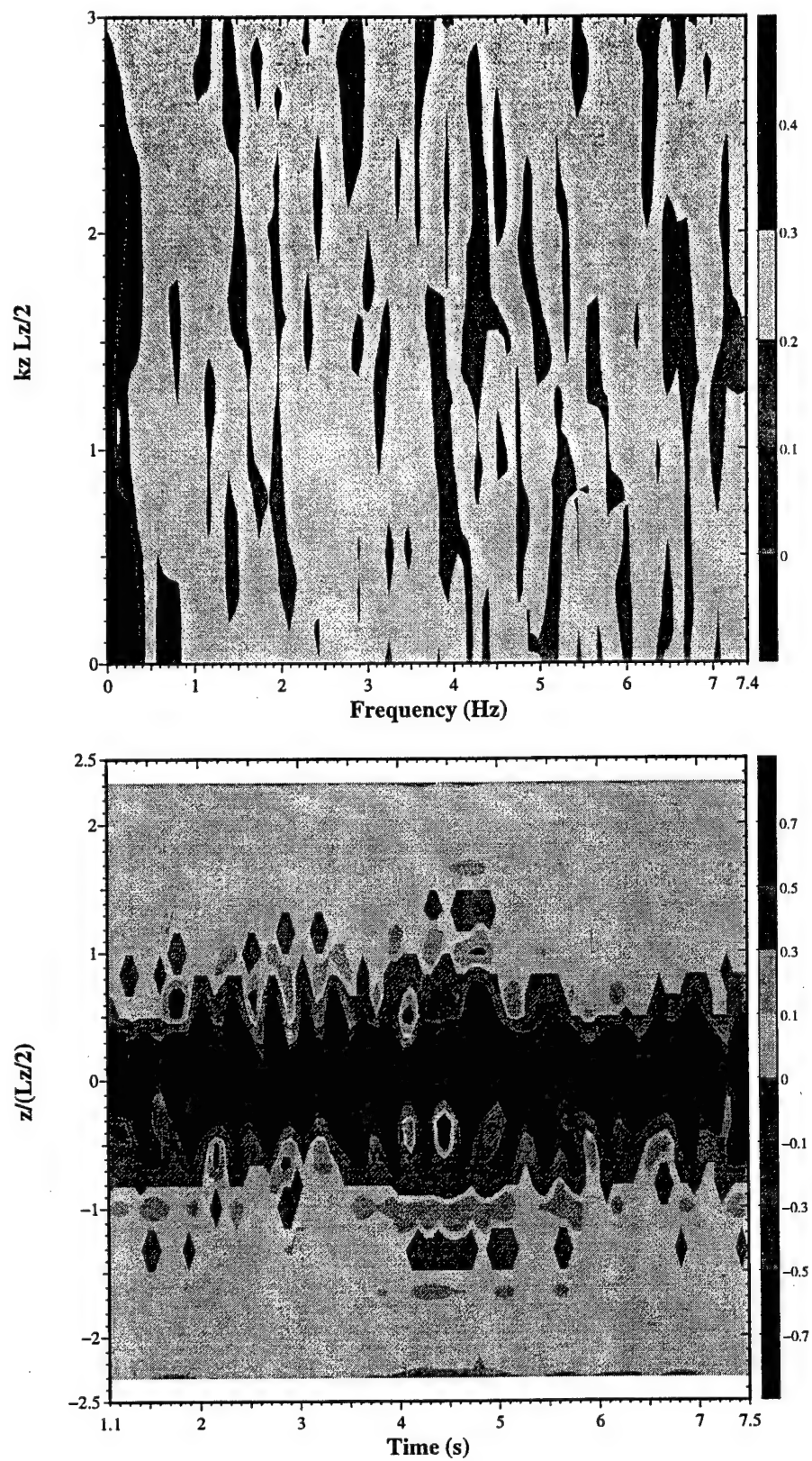
59

Figure 31: Frequency/spanwise wave number spectra (top) and sample time series (bottom) of wall pressure fluctuations in the boundary layer with 3-D mode forcing and actuators 5,8 & 11 at 90%.

4. Identifying optimum conditions for the actuators to alter these dominant modes.

The development of the optical pressure transducer was by far the most challenging part of the program. Ultimately it led to the use of a shear interferometer optical setup which provided the necessary adjustment to achieve sufficient sensitivity to detect changes in the spacing of the slope fringes. The manufacture of the reflective flexible membrane was found to be quite difficult. It ultimately became a balance between the mechanical properties, thickness, amount of applied tension, and the ability of the surface to be coated with a reflective metal. In the end we settled on two materials: either nitrocellulose or silicon. We tabulated suitable pressure ranges and thickness where either was appropriate. For the pressure range of the experiment, we chose to use a 1.5micron ($\pm 0.1 \mu$m) thick nitrocellulose membrane.

Although the membrane was bonded to the pressure disk surface with high precision, the high sensitivity of the measurements did reveal slight imperfections in the fringe patterns over some of the sensor holes. This made conventional methods for determining the fringe spacing less precise. As a result we developed a method based on a back-propagation neural network. The network was trained to distinguish the correct fringe pattern even when some distortion existed. It then categorized these into different pressure levels based on previous calibration runs. The error in the pressure reading was determined to be less than 10%.

We utilized a spanwise array of hot-wires as a second sensor arrangement for comparison to the optical pressure sensor. The hot-wires were placed at a fixed height above the boundary layer wall where they would be sensitive to changes in

the mean flow which were associated with nonlinear mean flow distortions produced by the growth of the input 3-D mode. These corresponded to standing patterns which were periodic in the spanwise direction with wave lengths of λ_{z3-D}, $\lambda_{z3-D}/2$ and $\lambda_{z3-D}/4$. The second of these was associated with the streamwise vortex mode which we were interested in affecting by the actuators. The mean flow distortion resulted in a spanwise variation in the integral thickness of the boundary layer. These were sensed by the hot-wire array and converted into an indicator function. In addition we performed 2-D frequency/wavenumber spectral analysis on the time series. From this we were able to identify the amplitudes of the different modes on the basis of their frequency and spanwise wave number (wave length). These were analyzed to determine the effect of the different actuator amplitudes, and spanwise configuration.

The results of the actuator study indicated that a single actuator located near the spanwise location of a 3-D mode amplitude maximum was effective in stabilizing the boundary layer. The results indicated that the actuator deflections needed to be in the range from approximately 8% to 16% of the boundary layer thickness. Within this range, there was approximately a linear relation between the amplitude and the mean indicator function. Below 8%, there was a minimum effect. Above 16%, any additional amplitude did not produce any change in the mean indicator function.

Raising a single actuator at the spanwise location of the 3-D mode amplitude minima had a minimal effect, even at the largest amplitudes. This indicates that an active control scheme needs to be able to identify the spanwise locations of the

62

amplitude maxima produced by the 3-D mode amplitude.

As an alternative to using a single actuator, we also investigated using multiple actuators. 42 combinations were considered. One of the most promising involved 3 actuators which were spaced $\lambda_{z_{3-D}}/4$ apart. This was expected to enforce a spanwise variation of the mean flow with wave lengths of $\lambda_{z_{3-D}}/4$ and $\lambda_{z_{3-D}}/2$. This arrangement was also effective in stabilizing the boundary layer, although 2-D spectral analysis revealed that the streamwise vortex mode amplitude increased. The advantage of using 3 actuators is that it is less sensitive to their spanwise location with respect to the initial 3-D mode structure. The disadvantage is that it is not as effective as a single actuator placed at the amplitude maximum, and there is more of a penalty in terms of the greater power required to raise three actuators versus one, and in the added drag produced by the added wall surface with three deflected elements versus one.

The results from the optical pressure sensor was consistent with those from the hot-wire array. This indicates that this non-intrusive measurement technique could be used to identify the optimum location to raise a single actuator, and to access the outcome on the flow. The optical setup was designed so that it could be implemented using fiber optics. This would allow the optics to be installed and viewed from inside a wing, rather than from the outside as was done in the laboratory. This approach, in conjunction with the actuator array, would make boundary layer control on an aerodynamic surface practical.

10 Bibliography

Balakumar, P. and Malik, M. 1990. Traveling disturbances in rotating-disk flow. *Theor. and Comp. Fluid Mech.*, **2**, 125-137.

Bassom, A. and Hall, P. 1989. On the interaction of stationary crossflow vortices and tollmien-schlichting waves in the boundary layer on a rotating disk. NASA contractor report 181159.

Bassom, A. and Hall, P. 1990. Concerning the interaction of non-stationary crossflow vortices in a three-dimensional boundary layer. NASA contractor report 182037.

Bassom, A. and Otto, S. 1992. On the stability of nonlinear viscous vortices in three- dimensional boundary layers.

Bassom, A. and Seddougui, S. 1989. A note concerning the onset of three dimensionality and time dependence on Gortler vortices. NASA contractor report 181956.

Corke, T. C. and Gruber, S. 1996. Resonant growth of three-dimensional modes in Falkner-Skan boundary layers with adverse pressure gradients. *J. Fluid Mech.*, **320**, 211-233.

Corke, T. and Mangano, R. 1989. Resonant growth of three-dimensional modes in transitioning Blasius boundary layers, *J. Fluid Mech.*, **209**, 93-150.

Corke, T., Krull, J. and Ghassemi, M. 1992. Three-dimensional mode resonance in far wakes. *J. Fluid Mech.*, **239**, 99-132.

Ghassemi, M. 1992. Secondary growth of 3-D modes in plane wakes. Ph.D. Thesis, Ill. Inst. of Tech.

Hall, P. and Horseman, N. 1990. The inviscid instability of fully nonlinear longitudinal vortex structures in growing boundary layers. ICASE report 90-71.

Hall P. and Smith F. 1991. On strongly nonlinear vortex/wave interactions in boundary layer transition. *J. Fluid Mech.*, bf 227, 641-666.

Herbert, Th. 1988. Secondary instabilities of boundary layers. *Ann. Rev. Fluid Mech.*, **20**, 487-526.

Kohama, Y. 1984. Study of boundary layer transition of a rotating disk. *Acta Mechanica*, **50**, Springer-Verlag, 193-199.

Malik, M. Wilkinson, S. and Orszag, S. 1981. Instability and transition in rotating disk flow. *AIAA J.*, **19**, 9, 1131-1138.

Mankbadi, R. 1992. A critical layer analysis of the resonant triad in Blasius boundary layer transition. Part II. Composite solution and comparison with observations. *J. Fluid Mech.*

Peto, J. A. 1997. Low mass magnetic actuators for wall surface disturbance of streamwise vortices. M.S., Illinois Institute of Technology.

Piroozan, P. 1997. Pressure sensor to determine spatial pressure distribution in boundary layer flows. Ph.D., Illinois Institute of Technology.

Speer, A. C. 1997. Spanwise analysis of velocity fluctuations in subharmonic transition. M.S., Illinois Institute of Technology.